INVESTIGATION OF PRECISE NEEDLE INSERTION FOR PROSTATE BRACHYTHERAPY

by

Carl Sylvester McGill

A dissertation submitted in partial fulfillment
of the requirements for the degree of
Doctor of Philosophy
(Biomedical Engineering)
in The University of Michigan
2012

Doctoral Committee:

<div style="margin-left:2em">

Professor Albert J. Shih, Co-Chair
Associate Professor Joseph L. Bull, Co-Chair
Professor Patrick W. McLaughlin
Associate Professor Jan P. Stegemann

</div>

DEDICATION

This dissertation is dedicated to my family and the long road we have travelled together to get to this point in my life. Thank you Charles (father) and Johnette (mother) for all the hard work and sacrifices that were made in order to provide a better life for your two boys. Thank you Curt for the continue support and encouragement throughout my graduate career. We did it. I love you all.

I would also like to dedicate this dissertation to Uncle "Gus" Carr. You were with me at the beginning of this journey, but were unable to see me cross the finish line and obtain my PhD degree. I know you are in a better place. I miss you.

ACKNOWLEDGEMENTS

First, I would like to thank my research advisor, Professor Albert Shih, for his guidance and willingness to continue exploring biomedical related research topic. Throughout this journey, he offered initial research suggestions while sharing his knowledge of successful grant and paper writing. I appreciate the time and effort you provided for me as I learned and performed prostate brachytherapy related research within your lab.

Also, I would like to thank my co-advisor, Professor Joseph Bull. From being my academic advisor as a master's student, to helping steer my research as a PhD student, you were always supportive in all of my pursuits. His door was always open, whether it was to share research ideas or just to talk about life and/or career goals. I appreciate everything you have done for me, related to my research and my professional development.

Also, I would like to thank my other committee members Dr. Patrick McLaughlin, M.D. and Professor Jan Stegemann for their insight, knowledge, and feedback throughout my graduate career. Dr. Patrick McLaughlin was always willing to try new ideas en route to helping improve the current prostate brachytherapy procedure. Thank you for your clinical expertise and time as we introduced new ideas, methods, and equipment into this field. Professor Jan Stegemann was always willing to bounce ideas, track my research progress, and share his knowledge with me.

Some of this work would have not been possible without the help of several individuals within the Sam Wu lab. Thank you Jason Moore, my needle lab partner, for the constant sharing of ideas as we learned about needle related research together. I would like to thank Jonathon Schwartz for his willingness to help me perform needle insertion experiments and for sharing his statistical knowledge. Thanks to Bruce (Li-Jung) Tai for his countless hours in teaching me the ins and outs of ABAQUS/CAE software and answering my numerous questions as it relates to finite element analysis.

TABLE OF CONTENTS

LIST OF FIGURES

LIST OF TABLES

LIST OF APPENDICES

ABSTRACT

This research investigates needle insertion through soft tissue, enabling the development and validation of force models and insertion techniques for accurate needle tip placement. During needle insertion into the prostate, the needle deflects en route to the target which leads to seed misplacement and suboptimal dose to cancerous cells. Many researchers have studied slow needle insertion speed and axial - needle insertion direction - force distribution and components. However, little work has been performed on stiffer needle material properties, tissue deformation with needle deflection, and normal - perpendicular to needle insertion direction - force distribution. This lack of knowledge have led to tissue deformation, needle deflection, and misplaced target when performing needle insertion procedures.

This research aims to quantify the impact of an optimized needle grid, insertion techniques, and needle-tissue force interaction leading to needle deflection and phantom deformation. First, an improved grid used to guide the needle was investigated and inserted via different hand insertion techniques to acquire needle deflection. To measure needle deflection, a measurement apparatus with acceptable gauge repeatability and reproducibility (GR&R) and documented accuracy was introduced. Next, stiffer needle properties were explored and inserted at much faster speed via a high-speed device, when compared to hand insertion or current robotic devices. Finally, finite element analysis (FEA) models were developed to predict relative needle-phantom motion using measured force data, while simultaneously obtaining experimental needle deflection and phantom

deformation. The needle and phantom FEA models and the normal force distribution on the needle shaft were validated with separate experimental results. Findings from this dissertation include a 40% decrease in average needle deflection with the improved grid (and the same fast hand insertion technique), in addition to a 60% decrease in average needle deflection with the stiffer needle at the faster speed (compared to the less stiff needle and slow speed). Also, the needle and phantom FEA models are reasonably accurate to the experimental data, having a difference of 7% and 18%, respectively. These findings can be used to improve needle insertion techniques, while understanding force distribution effect on needle bending and compensate during the insertion path.

CHAPTER 1

INTRODUCTION

1.1 RESEARCH MOTIVATION

Prostate cancer is the second most frequently diagnosed cancer and the second-leading cause of cancer death in men [1]. During 2012, the American Cancer Society estimated that 241,740 new cases will occur in the United States. Prostate-specific antigen (PSA) test has enabled the early detection of prostate cancer via measuring the level of proteins, produced by the cells of the prostate gland, in the blood. Although elevated levels (above 4.0 ng/mL) require monitoring, PSA test does not confirm prostate cancer since many benign conditions, such as enlargement or inflammation, can increase PSA levels [2]. After confirming prostate cancer, usually by a needle biopsy, brachytherapy could be one of the treatment methods. Brachytherapy is the placement of radioactive seeds into the prostate gland via a needle and it has become an increasingly popular treatment for prostate cancer when it is detected in the early stages [3-5].

In brachytherapy (Figs. 1.1 and 1.2), about 50 to 150 radioactive seeds, 0.8 mm in diameter and 4.5 mm in length, are permanently placed into the prostate [6,7]. Around 15 to 35 needles, typically 18-gauge, are inserted into the walnut size prostate for radioactive seeds placement. In the transrectal ultrasound (TRUS) procedure (Fig. 1.1), the ultrasound probe is used to create an image of the prostate and confirm needle insertion placement [6,7]. The grid, which is attached to the set-up, allows the surgeon to insert the needle at specified targets. Once the implanted seeds are position within the prostate, they are not easily seen by ultrasound, thus X-Ray (Fig. 1.2) is needed to confirm radioactive seed placement. The radiation dose provided by each seed covers a certain tissue volume adjacent to the seed.

Position accuracy of the radioactive seeds into the prostate is important for optimizing the dose delivery to cancerous tissue along with sparing critical organs and structures [7-9]. However, during needle insertion into the prostate, the needle deflects en route to the target. Precise insertion of needles is challenging due to tissue heterogeneity and low elastic stiffness, tissue deformation, unfavorable anatomic structures via the pubic arch interference, and poor maneuverability [7-10]. Misplaced seeds can result in negative side effects such as urinary and bowel incontinence, rectal bleeding, erectile dysfunction, and vital tissue damage [7-9].

This research aims to decrease needle deflection en route to the target within the tissue. Different techniques are developed in addition to designing and optimizing current prostate brachytherapy equipment. Additionally, a finite element model is developed to predict needle deflection and phantom deformation.
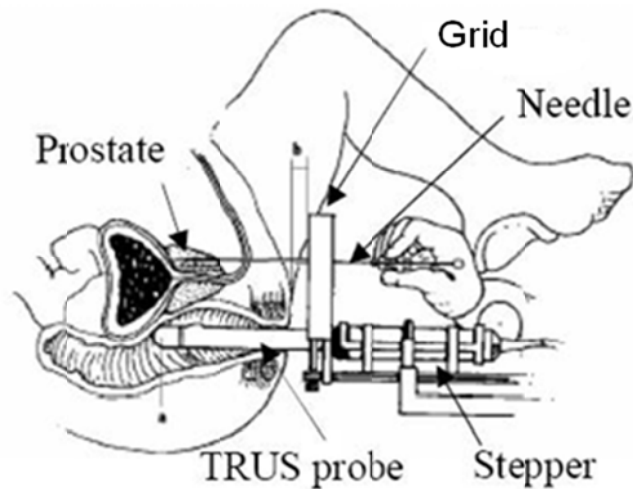
Figure 1.1. Transrectal Ultrasound (TRUS) prostate brachytherapy [10]
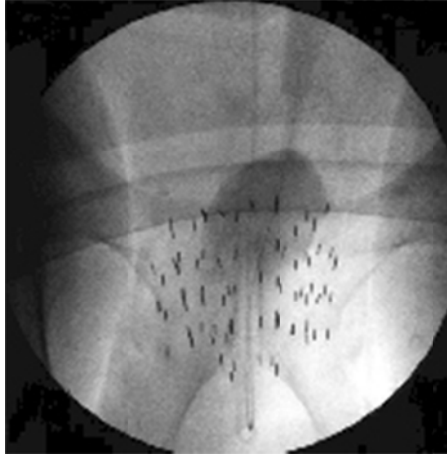
Figure 1.2. X-ray of radioactive seeds during the prostate brachytherapy procedure [11]

1.2 LITERATURE REVIEW

1.2.1 Needle insertion force and speed measurement

Podder et al. [12] performed *in vivo* measurements of the needle insertion force and motion trajectory during prostate brachytherapy in the operating room. Results showed that the overall maximum average needle insertion force was significant lower for an 18 gauge, compared to a 17 gauge needle. Additionally the authors attributed variations in traverse forces to factors such as tissue heterogeneity, movement of internal organs, and lateral movement of the surgeon's hand while operating the needle. These factors also contributed to needle deflection from the desired trajectory and target movement. Kataoka et al. [13] measured the tip and friction forces (axial force) independently acting on a needle during insertion into a canine prostate via a seven-axis load cell. Results from the insertion test imply that the friction force was generated uniformly along the axis by the constant clamping force (forces perpendicular to the needle insertion direction). Okamura et al. [14] developed empirical models by separating the needle insertion (axial) force into three parts: stiffness, friction, and cutting forces. The stiffness force, which occurred before puncture of the capsule, was modeled as a non-linear spring model. After the puncture, the friction and cutting forces were

3

modeled as a modified Karnopp model [15] and a constant for a given tissue, respectively.

The effect of needle speed during insertion was explored by several researchers in order to reduce needle deflection. Podder et al. [16] performed experiments on phantoms at various insertion speed, needle oscillations, and needle rotation. Results show that axial force increases as speed increases, leading to an increase in target movement. Low frequency oscillation increases the force and target deflection. Higher needle rotation does decrease tissue deformation as long as the rotational speed is high enough to counteract the deformation created by the higher insertion speed. Yan et al. [17] investigated high frequency (20 kHz vs. 2 kHz) translational oscillation along with rotation of the needle on phantoms and chicken breast tissue. High frequency translational oscillation reduces phantom deformation by more than twice the low frequency. Rotational drilling reduced target movement, as compared to no rotation during needle insertion.

1.2.2 Needle insertion modeling, imaging modalities, and deflection measurement

Modeling techniques were used to simulate and optimize brachytherapy seed placement error. Jiang et al. [18] constructed a 3D non-linear dynamic finite element model (FEM) numerical algorithm used in combination with the Mooney-Rivlin material model, to accommodate the non-linear mechanical and geometrical behavior of the human tissue. After performing experiments to test the sensitivity of seed placement error with insertion point, needle orientation, and insertion distance, the authors concluded that smaller placement error occurs when the distance between the insertion point and target is shorter. Likewise, Dehghan et al. [19] optimized the needle insertion point, velocity, and depth using a neo-Hookean non-linear material prostate model and needle insertion simulation to minimize seed misplacement error.

Using 25 patients' data, Podder et al. [20] developed a statistical model from procedure-specific criteria and patient-specific criteria to estimate the maximum force that the needle inserts on the patient. Procedure-specific *in vivo* data included size,

speed, and acceleration of the needle and patient-specific criteria consisted of nine categories including age, body mass index (BMI), ethnicity, and prostate volume. Furthermore, Glozman et al. [21,22] developed a model for flexible needle steering into viscoelastic materials via path planning and optimization for minimal tissue pressure. The tissue forces on the needles were modeled as lateral virtual springs along the needle curve with friction forces tangent to the needles. A robot [21,23] verified the proposed concept by maneuvering the needle base and inserting the needle into animal tissues.

Robotic-assisted tools have been utilized to increase needle placement accuracy. Using a two degree-of-freedom (DOF) robot for needle insertion, Abolhassani et al. [24] presented an analytic model to estimate needle deflection, while modeling the needle as a flexible beam with support. This model incorporates force and moment at the needle base, in conjunction with angle of the bevel and cutting force at the tip. Wan et al. [25] used a robot with 6-DOF to test several insertion methods, including constant orientation, constant rotation, and orientation reversal at half of the insertion depth on needle deflection. 3D TRUS images were obtained to calculate the error between the needle tip and planned position; analysis via MATLAB produced the population distribution of the displacement in 3D. Meltsner et al. [26] focused on optimizing parameters such as needle type (beveled versus conical), insertion speed, and needle rotation speed while experimenting with a 6-DOF robot. Minimize tissue damage while still maintaining reduced force with increased accuracy was obtained with the rotate-cannula-only method of the conical needle.

Imaging modality was also used as an aid in needle insertion. DiMaio et al. [27] portrayed a system that integrates an image-based target planning interface. A robotic placement mechanism is used for remote manipulation of the needle in MRI without moving the patient out of the imaging space, as well as robot and needle tracking for navigation and control. A leg support created a "tunnel" that enabled the robotic needle driver to perform the brachytherapy procedure while the patient stayed in the MRI. Tatli et al. [28] described a brachytherapy procedure using a vertically open configuration MRI system with the patient in the lithotomy position under general anesthesia. Since MRI does not dissipate any ionizing radiation, interventional radiologist can stand alongside patients throughout the procedure when an open configuration MRI system is used. In

contrast, most open MRI carries either low or midfield magnetic strength which results in anatomic details to be lost or lack of tumor visualization

Many methods have been developed to measure needle deflection during experimentation. Kataoka et al. [29] used a bi-plane X-Ray imaging system to reconstruct the shape of the needle after insertion into swine muscle. Blake et al. [30] investigated the use of 3D ultrasound (both tilt and pull-back scanning) for brachytherapy seeds localization. CT and a stereotactic head frame were used to confirm a match between the ultrasound and CT coordinate images. To measure final deflection within a phantom, graph paper was pasted on each ends of the phantom block and the initial insertion hole was used as the reference. Abolhassani et al. [24,31] used a sensor coil, part of a magnetic tracking system, to follow the needle tip position.

1.3 RESEARCH OBJECTIVES

The scope of this research is to develop precise needle insertion techniques and optimize current equipment used in prostate brachytherapy procedures. As discussed above in the motivation (Section 1.1), during needle insertion into the prostate, the needle deflects en route to the target which leads to seed misplacement and suboptimal dose to cancerous cells. Specific objectives of this research are as follow:

a) Develop and optimize the needle grid inside diameter hole and overall length; study the hand motion speed effect on needle insertion accuracy; and design a measurement system that has acceptable gauge repeatability and reproducibility.

b) Investigate the effect of trocar (inner solid portion of the needle) stiffness on needle deflection and explore the effect of high-speed (pneumatic) needle insertion.

c) Propose a finite element force model and validate results from measured experimental data. Validate the needle normal distribution force present during insertion.

1.4 ORGANIZATION OF THE DISSERTATION

This dissertation is presented in a multiple manuscript format for Chapters 2, 3, and 4. Each chapter (2, 3, 4) correlates to each research objective listed in Section 1.3.

Chapter 1 provides the overall motivation for this dissertation research, in addition to a literature review that relates to this dissertation research objectives.

Chapter 2 presents the improved needle grid with reduced diametral clearance between the grid inside diameter hole and outside diameter needle, in addition to the increased grid length for the needle to have a longer travel distance before insertion into the tissue. A measurement system, with acceptable GR&R results, was developed to calculate final needle deflection without using image modality. Also, fast versus slow hand needle insertion speed is investigated.

Chapter 3 investigates the material properties of the trocar by experimenting with a higher Young's modulus material (compared to what is currently used) inserted at very high-speed via a pneumatic device.

Chapter 4 develops a finite element model for needle deflection and phantom deformation. Three directional needle-tissue interaction forces were measured while simultaneously acquiring needle deflection and phantom deformation data. Both the model and the needle normal distribution force were validated with experimental results.

Chapter 5 summarizes this dissertation, potential future work for this field, and the author's original contributions.

REFERENCES

1. American Cancer Society. Cancer Facts & Figures 2012. Atlanta: American Cancer Society; 2012.

2. *Prostate-Specific Antigen (PSA) Test*, National Cancer Institute, NIH, DHHS, Bethesda, MD, 2012, http://www.cancer.gov/cancertopics/factsheet/detection/PSA.

3. J. D. Hall, J. C. Boyd, M. C. Lippert, and D. Theodorescu, "Why patients choose prostatectomy or brachytherapy for localized prostate cancer: results of a descriptive survey," Urology **61**, 402-407 (2003).

4. J. J. Coen and A. L. Zietman, "Proton radiation for localized prostate cancer", Nature Reviews Urology **6**, 324-330 (2009).

5. M. R. Cooperberg, D. P. Lubeck, M. V. Meng, S. S. Mehta, and P R. Carroll, "The changing face of low-risk prostate cancer: trends in clinical presentation and primary management," Journal of Clinical Oncology **22**, 2141-2149 (2004).

6. A. T. Porter, J. C. Blasko, P. D. Grimm, S. M. Reddy, and H. Ragde, "Brachytherapy for prostate cancer," CA: A Cancer Journal for Clinicians **45**, 165-178 (1995).

7. J. C. Blasko, T. Mate, J. E. Sylvester, P. D. Grimm, and W. Cavangah, "Brachytherapy for carcinoma of the prostate: techniques, patient selection, and clinical outcomes," Seminars in Radiation Oncology **12,** 81-94 (2002).

8. S. Nath, Z. Chen, N. Yue, S. Trumpore, and R. Peshcel, "Dosimetric effects of needle divergence in prostate seed implant using ^{125}I and ^{103}Pd radioactive seeds," Medical Physics **27**, 1058-1066 (2000).

9. N. N. Stone and R. G. Stock, "Complications following permanent prostate brachytherapy," European Urology **41**, 427-433 (2002).

10. T. K. Podder, W. S. Ng, and Y. Yu, "Multi-channel robotic system for prostate brachytherapy," *29th Annual International Conference of the IEEE Engineering in Medicine and Biology Society*, (Lyon, France, 2007), pp. 1233–1236.

11. *Brachytherapy*, Prostate Cancer Centre Network, Guildford, Surrey GU2 7RF, UK, 2012. http://www.prostatespecialist.co.uk/main_pages/main_brachy.htm**.**

12. T. K. Podder, D. P. Clark, J. Sherman, D. Fuller, E. Messing, D. Rubens, J. Strang, R. Brasacchio, L. Liao, W. S. Ng, and Y. Yu, "*In vivo* motion and force measurement of

surgical needle intervention during prostate brachytherapy," Medical Physics **33**, 2915-2922 (2006).

13. H. Kataoka, T. Washio, K. Chinzei, K. Mizuhara, C. Simone, and A. M. Okamura, "Measurement of the tip and fiction force acting on a needle during penetration," *Proceedings of the 5th International Conference on Medical Image Computing and Computer-Assisted Intervention* — MICCAI (Tokyo, Japan, 2002), pp. 216-223.

14. A. M. Okamura, C. Simone, and M. D. O'Leary, "Force modeling for needle insertion into soft tissue," IEEE Trans. Biomed. Eng. **51**, 1707–1716 (2004).

15. D. Karnopp, "Computer simulation of stick-slip friction in mechanical dynamic systems," Journal of Dynamic Systems, Measurement, and Control **107,** 100-103 (1985).

16. T. K. Podder, D. P. Clark, D. Fuller, J. Sherman, W. S. Ng, L. Liao, D. Rubens, J. Strang, E. Messing, Y. D. Zhang, and Y. Yu, "Effects of velocity modulation during surgical needle insertion," *27th Annual International Conference of the IEEE Engineering in Medicine and Biology Society*, (Shanghai, China, 2005), pp. 5766–5770.

17. K. Yan, W. S. Ng, K. V. Ling, T. Liu, Y. Yu, and T. K. Podder, "High frequency translational oscillation & rotational drilling of the needle in reducing target movement," *IEEE International Symposium on Computational Intelligence in Robotics and Automation*, (Espoo, Finland, 2005), pp. 163-168.

18. S. Jiang, N. Hata, and R. Kikinis, "Needle insertion simulation for image-guided brachytherapy of prostate cancer," *2nd International Conference on Bioinformatics and Biomedical Engineering*, (Shanghai, China, 2008), pp. 1682-1685.

19. E. Dehghan and S. E. Salcudean, "Needle insertion point and orientation optimization in non-linear tissue with application to brachytherapy," *IEEE International Conference on Robotics and Automation,* (Rome, Italy, 2007), pp. 2267-2272.

20. T. K. Podder, J. Sherman, E. M. Messing, D. J. Rubens, D. Fuller, J. G. Strang, R. A.Brasacchio, and Y. Yu, "Needle insertion force estimation model using procedure-specific and patient-specific criteria," *28th Annual International Conference of the IEEE Engineering in Medicine and Biology Society,* (New York City, USA, 2006) pp. 555-558.

21. D. Glozman and M. Shoham,"Flexible needle steering for percutaneous therapies," Computer Aided Surgery **11,** 194–201 (2006).

22. D. Glozman and M. Shoham, "Flexible needle steering and optimal trajectory planning for percutaneous therapies," *Proceedings of the 7th International Conference on Medical Image Computing and Computer-Assisted Intervention – MICCAI* (Saint-Malo, France, 2004), pp. 137-144.

23. J. R. Crouch, C. M. Schneider, J. Wainer, and A. M. Okamura, "A velocity-dependent model for needle insertion in soft tissue," *Proceedings of the 8th International Conference on Medical Image Computing and Computer-Assisted Intervention – MICCAI,* (Palm Springs, CA, 2005), pp. 624-632.

24. N. Abolhassani, R. V. Patel, and F. Farzam, "Minimization of needle deflection in robot-assisted percutaneous therapy," The International Journal of Medical Robotics and Computer Assisted Surgery **3**, 140-148 (2007).

25. G. Wan, Z. Wei, L. Gardi, D. B. Downey, and A. Fenster, "Brachytherapy needle deflection evaluation and correction," Medical Physics **32**, 902-909 (2005).

26. M. A. Meltsner, N. J. Ferrier, and B. R. Thomadsen, "Observations on rotating needle insertions using a brachytherapy robot," Physics in Medicine and Biology **52**, 6027-6037 (2007).

27. S. P. DiMaio, G. S. Fischer, S. J. Haker, N. Hata, I. Iordachita, C. M. Tempany, R. Kikinis, and G. Fichtinger, "A system for MRI-guided prostate interventions," IEEE/RAS-EMBS International Conference on Biomedical Robotics and Biomechatronics (2006) pp. 68-73.

28. S. Tatli, P. R. Morrison, K. Tuncali and S. G. Silverman, "Interventional MRI for oncologic applications," Techniques in Vascular and Interventional Radiology **10**, 159-170 (2007).

29. H. Kataoka, T. Washio, M. Audette, and K. Mizuhara, "A Model for relations between needle deflection, force, and thickness on needle penetration," *Proceedings of the 4th International Conference on Medical Image Computing and Computer-Assisted Intervention,* (Utrecht, The Netherlands, 2001), pp. 966–974.

30. C. C. Blake, T. L. Elliot, P. J. Slomka, D. B. Downey, and A. Fenster, "Variability and accuracy of measurements of prostate brachytherapy seed position *in vitro* using

three-dimensional ultrasound: An intra- and inter-observer study," Medical Physics **27,** 2788-2795 (2000).

31. N. Abolhassani, R. Patel, and F. Ayazi, "Effects of different insertion methods on reducing needle deflection," *29th Annual International Conference of the IEEE Engineering in Medicine and Biology Society*, (Lyon, France, 2007), pp. 491–494.

CHAPTER 2

PRECISION GRID AND HAND MOTION FOR ACCURATE NEEDLE INSERTION IN BRACHYTHERAPY

ABSTRACT

In prostate brachytherapy, a grid is used to guide a needle tip towards a pre-planned location within the tissue. During insertion, the needle deflects en route resulting in target misplacement. In this paper, 18-gauge needle insertion experiments into phantom were performed to test effects of three parameters, which include the clearance between the grid hole and needle, the thickness of the grid, and the needle insertion speed. Measurement apparatus that consisted of two datum surfaces and digital depth gauge was developed to quantify needle deflections. The gauge repeatability and reproducibility (GR&R) test was performed on the measurement apparatus and it proved to be capable of measuring a 2 mm tolerance from the target. Replicated experiments were performed on a 2^3 factorial design (3 parameters at 2 levels) and analysis included averages and standard deviation along with an analysis of variance (ANOVA) to find significant single and two-way interaction factors. Results showed that grid with tight clearance hole and slow needle speed increased precision and accuracy of needle insertion. The tight grid was vital to enhance precision and accuracy of needle insertion

for both slow and fast insertion speed; additionally, at slow speed the tight, thick grid improved needle precision and accuracy. In summary, the tight grid is important, regardless of speed. The grid design, which shows the capability to reduce the needle deflection in brachytherapy procedures, can potentially be implemented in the brachytherapy procedure.

2.1 INTRODUCTION

Position accuracy of the needle tip to place the radioactive seeds into the prostate is important for optimizing the dose delivery and efficacy to cancerous tissue. This treatment, called brachytherapy, is performed to eradicate cancerous cells within the prostate gland. Inaccurately placed seeds can result in adverse side effects such as urinary and bowel incontinence, rectal bleeding, erectile dysfunction, and substantial tissue damage [1-3].

Accurate seed placement is determined by the placement of the needle tip in the tissue. Transperineal image-guided brachytherapy enables real-time localization of needle positioning [3,4]. A major problem experienced with this brachytherapy procedure is that the needle deflects en route to the target due to the inherent tissue deformation caused by soft and heterogeneous tissue properties, unfavorable anatomic structures in and around the prostate, and the limited maneuverability with needle insertion [1-3].

To improve the needle insertion accuracy in brachytherapy, investigators have studied the needle insertion process and prostate deformation in an attempt to model the needle-tissue interaction [5-7], to predict the needle deflection and the needle path based on measured needle insertion forces [8-13], and to improve the needle insertion accuracy through the use of a robotic-assisted tool [9,14-16]. Abolhassani [17] has an in-depth survey of the needle trajectories, tissue deformation modeling, and various other needle-tissue interaction properties during the needle insertion. To our knowledge no studies have been conducted on the effect of the grid, which supports the needle during insertion,

and speed of needle generated by hand motion and its outcome on the accuracy of needle placement.

In brachytherapy, the orientation of the needle during insertion is constrained by a grid, also referred to as a template [3,4]. A grid [18,19], as shown in Fig. 2.1(a), consists of an array of equally-spaced holes, which have the inside diameter closely matching the outside diameter of the needle. The 18 gauge needle, having a 1.270 ± 0.013 mm outer diameter, is commonly used during brachytherapy. The needle is guided by a hole in the grid into a pre-planned target location within the soft tissue. The needle grid (Civco Medical Solutions, IA), as shown in Fig. 2.1(a), is made of plastic and has a 13×13 array of holes. The spacing between adjacent holes is 5 mm and the thickness of the grid is 20.3 mm. The diametral clearance between the outside diameter of the needle and hole inside diameter of the current commercially available 18-gauge grid is about 76 μm, which is large from the precision engineering perspective. This study applies a precision reaming process to produce a stainless steel grid that has smaller and more consistent hole size for needle guidance. The diametral clearance between the new grid inside diameter hole and the outside diameter needle is reduced to 33 μm. One of the goals of this study is to investigate the effect of the reduction of this clearance on the accuracy of needle insertion.

In current brachytherapy procedures, physicians in radiation oncology manually insert the needle through the grid and into the prostate gland with a quick flick of the wrist to achieve a high-needle speed and less deflection of needle. Another goal is to study the effect of this hand motion in needle insertion on the accuracy of needle placement.

Quantifying needle deflection provides a means to compare and evaluate improvements on accuracy. Techniques used to measure deflection or track the needle path include reconstructing the stereo images of a bi-plane X-ray system [10], inserting inside the needle a five-degrees of freedom sensor coil that uses a magnetic field as part of the set-up [11,20], and placing graph papers on each ends of the phantom [21,22]. These methods do not have documented measurement accuracy. The well-established gauge repeatability and reproducibility (GR&R) [23-25] measurement test in precision metrology can quantify the error of these measurement techniques for needle deflection.

The final goal of this study is to design a measurement system that has acceptable GR&R results and documented accuracy on needle deflection measurements.
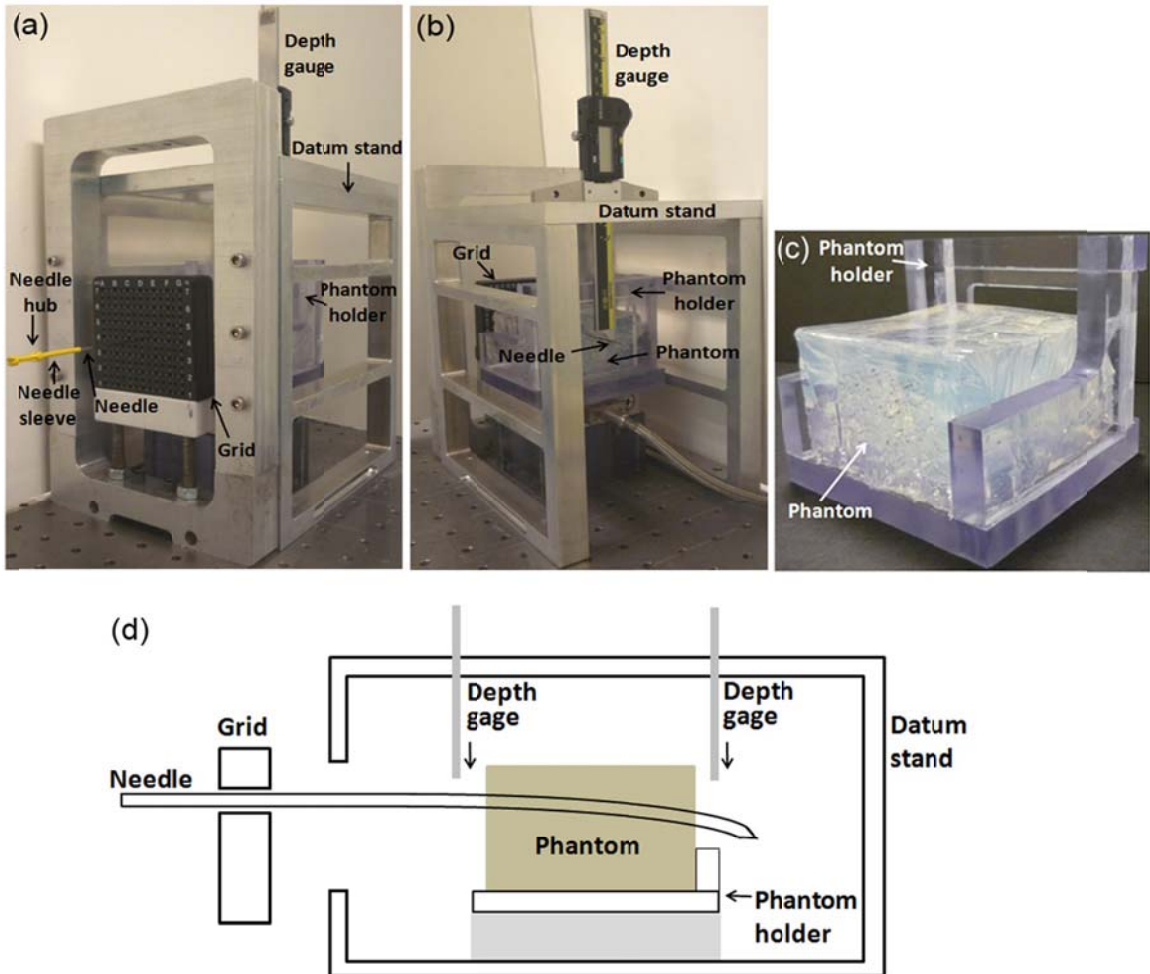
Figure 2.1. (a) Front-view and (b) rear-view of the experimental set-up which includes the grid, needle, phantom, phantom holder, measurement datum stand, and depth gauge. (c) Phantom holder and phantom with an opening on the back of the phantom holder that allows the needle to exit. (d) Schematic drawing of experimental set-up.

2.2 MATERIALS AND METHOD

2.2.1 Overview of experimental set-up

The set-up (Fig. 2.1) for the experiment includes a needle, phantom, phantom holder, grid, measurement datum stand, and digital depth gauge. The needle used throughout the experiment was the commonly used 18-gauge prostate brachytherapy needles (Model MTP-1820-C, Mick Radio-Nuclear Instruments Inc, NY). The brachytherapy needle consists of two main parts, the inner solid trocar and outside hollow cannula, both made of AISI 304 stainless steel. The trocar, which is the inner solid rod that converges to a diamond point (3-plane) at one tip, has a diameter of about 1.01 mm. Enclosing the trocar is the hollow cannula. At the opposite end of the diamond tip of the trocar is a yellow covering, called the hub [Fig. 2.1(a)]; likewise, there is also a yellow covering on the cannula opposite the tip, called the needle sleeve. The hub and needle sleeve provide a means to hold and insert the needle combination during the brachytherapy procedure. Bevel tip needles were not considered because diamond tip needles, commonly used in brachytherapy, produced less deflection when inserted in a similar homogenous phantom, as shown by Podder et al. [21].

The phantom was made of polyvinylchloride (PVC) modified with plastisol, previously used by Podder et al. [21,26], and was created from a 1:1 ratio of regular liquid plastic to plastic softener (M-F Manufacturing, TX). In order to have a consistent phantom specimen throughout the entire experiment, one batch of mixture was produced and cut into two separate phantom blocks with the stated dimensions. One phantom block was formed to have a length of 85 mm that the needle traveled through; this length was also used to measure needle deflection within the phantom. A width of 75 mm was molded to accommodate the phantom height of 50 mm. This width-height aspect ratio provided enough self-support for the phantom to stay on the phantom holder as well as enough space for needle insertion at several height levels of holes in the grid.

The phantom holder [Fig. 2.1(c)], 90 mm long × 100 mm wide × 75 mm high, was made from 12.7 mm thick polycarbonate and used to secure the phantom and provide a constant location to measure the needle for position coordinates. The phantom holder

16

encloses some of the phantom on the right and left sides and the entire phantom on the bottom. An opening on the back of the phantom holder allows the needle to exit the phantom during needle insertion. A constant distance of 25 ± 5 mm was set between the phantom and the front of each interchangeable grid for every needle insertion trial. This distance is a representative value of the gap between the patent's skin and the grid which is present during brachytherapy procedures.

The descriptions on the grids and measurement apparatus (datum stand and digital depth gauge) are explained in the next two sections, Sections 2.2.1.1 Grids and 2.2.1.2 Needle deflection measurement apparatus.

2.2.1.1 Grids

The two factors of interest related to the grid were the tightness of the hole and the length of the grids. Four sets of grids, as shown in Fig. 2.2, were used in the experiment. One is the plastic grid (Civco Medical Solutions, IA), as shown in Fig. 2.2(a), used in current brachytherapy procedures for 18-gauge needles. This grid, marked as the loose thin grid in Fig. 2.2(a) and Table 2.1, has a 13 × 13 array of equally-spaced 1.346 mm diameter holes and a thickness of 20.3 mm. Two plastic grids were stacked together to increase the thickness to 40.6 mm, which is marked as loose thick in Table 2.1 and shown in Fig. 2.2(b).

Metal grids with a 13 × 13 array of equally-spaced holes, the same configuration as the current plastic grid, were constructed. To determine the hole size of the metal grid for tighter diametral clearance, a set of holes with 6 μm size step was constructed for testing and selecting the suitable hole size. A radiation oncologist performed test insertions on this grid to feel and find the smallest hole that had the same level of resistance on the needle as the resistance encountered in the operating room when the needle is inserted for the brachytherapy procedure. The 1.303 mm hole diameter, marked as tight grids in Fig. 2.2 and Table 2.1, was selected. The diametral clearance between the 1.303 mm hole and the 18-gauge needle is about 33 μm.

The reaming tool to produce the precision hole has limited length and can only produce 12.7 mm deep hole. In this study, as shown in Figs. 2.2(c) and 2.2(d) and listed in Table 2.1, the tight thin and tight thick grids are the stacking of two and four of these precise holes 12.7 mm thick metal plates producing 25.4 mm and 50.8 mm thickness, respectively, using precision dowel pins and screws.
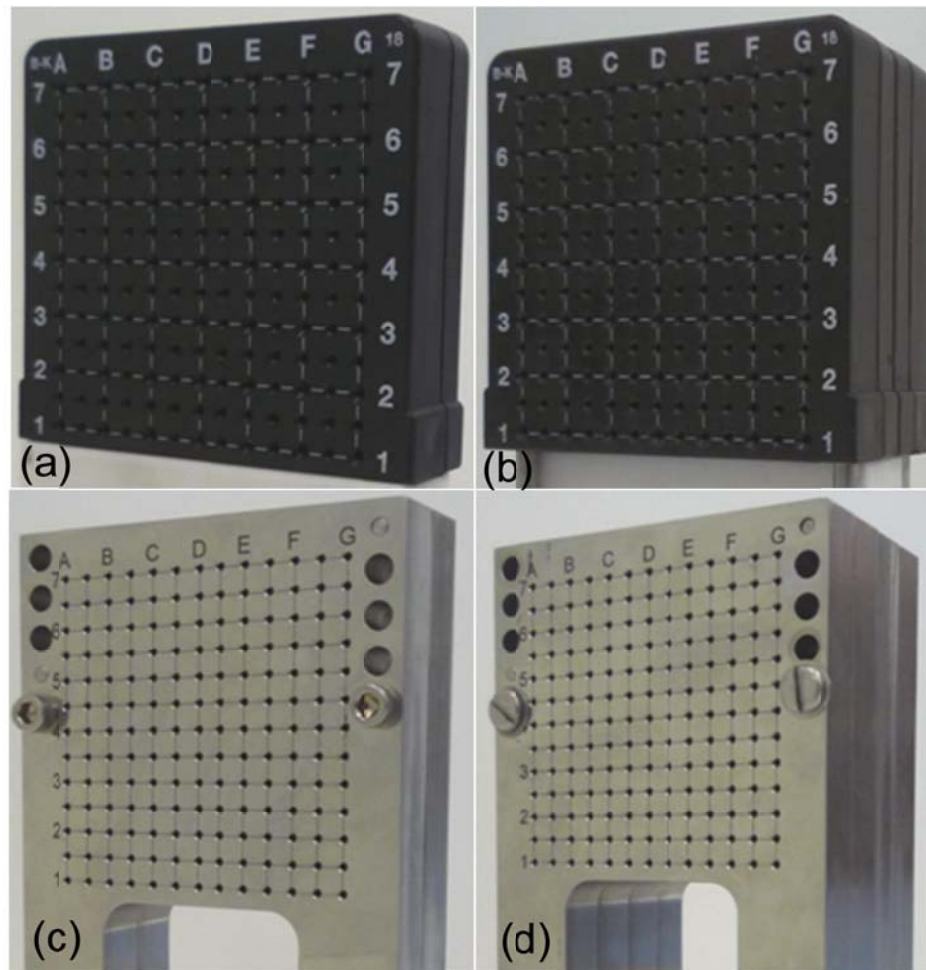
Figure 2.2. Grids – isometric view of the four (a) loose thin, (b) loose thick, (c) tight thin, and (d) tight thick grids in this study. (a) and (b) are the plastic grids with (c) and (d) are the 316 stainless steel metal grids.

Table 2.1. Specification of the four needle grids

Grid type	Grid thickness (mm)	Hole diameter (mm)
Loose thin	20.3	1.346
Loose thick	40.6	1.346
Tight thin	25.4	1.303
Tight thick	50.8	1.303

2.2.1.2 Needle deflection measurement apparatus

The measurement apparatus, as shown in Figs. 2.1(a) and 2.1(b), includes the datum stand, attached to the grid holder, and a digital depth gauge (Mitutoyo Model VDS-6 DCX) with 0.01 mm resolution. The same depth gauge was used to mechanically measure the needle position coordinates in the x- and y- directions from the x- and y-datum surfaces, as shown in Fig. 2.3. The x- and y-coordinates of the needle after it enters and exits the phantom are marked as (X_{enter}, Y_{enter}) and (X_{exit}, Y_{exit}), respectively, and measured using the same depth gauge, as illustrated in Fig. 2.3. The depth gauge base was parallel to the respective datum plane. The needle deflection through the 85 mm phantom length are denoted as $X_{deflection}$ and $Y_{deflection}$ and can be calculated using:

$$X_{deflection} = X_{enter} - X_{exit} \tag{2.1}$$

$$Y_{deflection} = Y_{enter} - Y_{exit} \tag{2.2}$$

The resultant/radial deflection (R) is:

$$R = \sqrt{X_{deflection}^2 + Y_{deflection}^2} \tag{2.3}$$
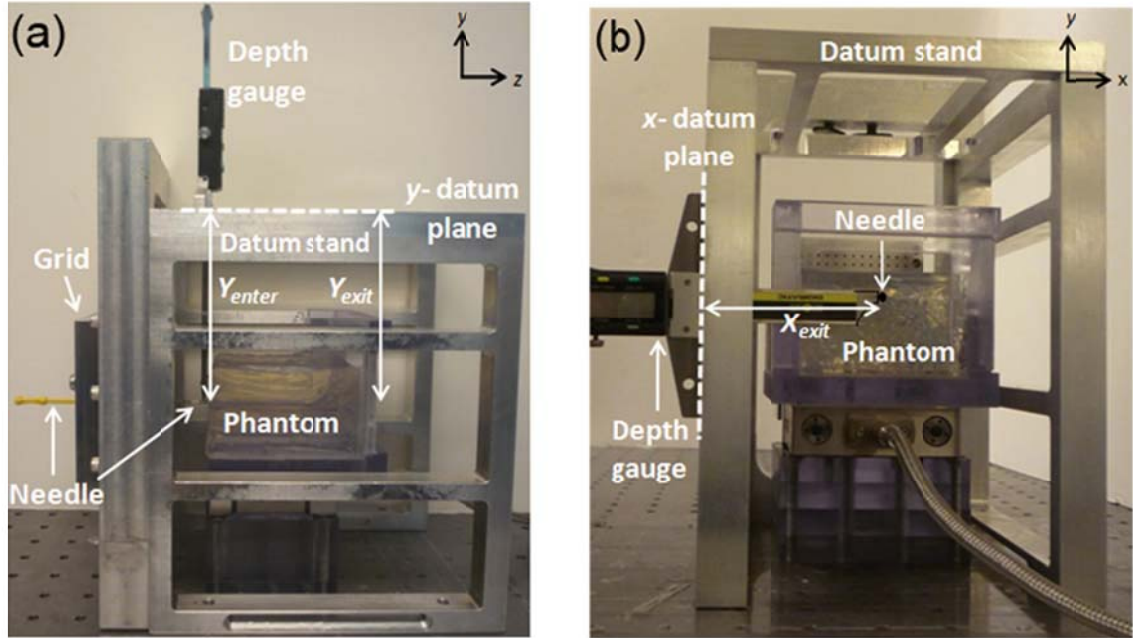
Figure 2.3. Needle deflection measurement apparatus with the datum stand, *x*- and *y*- datum planes, and precise digital depth gauge to measure the needle positions (a) side view of the needle, grid, depth gauge, *y*- datum plane and measured Y_{enter} and Y_{exit} and (b) back view of *x*- datum plane and measured X_{enter} and X_{exit}.

2.2.1.3 Needle insertion speed and phantom deformation

During the experiment, a needle was inserted by hand at a slow or fast speed through a hole on the grid and into the phantom. The fast speed is created by a quick flick of the wrist commonly used by radiation oncologists in the current hand placed needle insertion brachytherapy procedure. The operator's hand was placed behind the hand plate to push the hand plate and drive the needle to insert through the grid and into the phantom under the guidance of the hand plate. A linear optical encoder (Heidenhain Model Lida 277) was attached to the hand plate to measure the position of the needle during hand insertion, as shown in Fig. 2.4. The data was recorded using a data acquisition system (National Instruments Model NI DAQPad-6015) and Labview at a sampling rate of 50 kHz. The needle insertion speed was calculated based on the displacement and time data. The slow speed was 60 ± 40 mm/s, while the fast speed was 525 ± 60 mm/s for the loose thin, loose thick, and tight thin grids and 750 ± 60 mm/s for

the tight thick grid. Once inserted, the needle was measured for x- and y-coordinates at the entry and exit of the phantom to calculate the deflection. Measurements were repeated for each insertion. Phantom deformation at slow and fast needle insertion speeds were recorded using video.
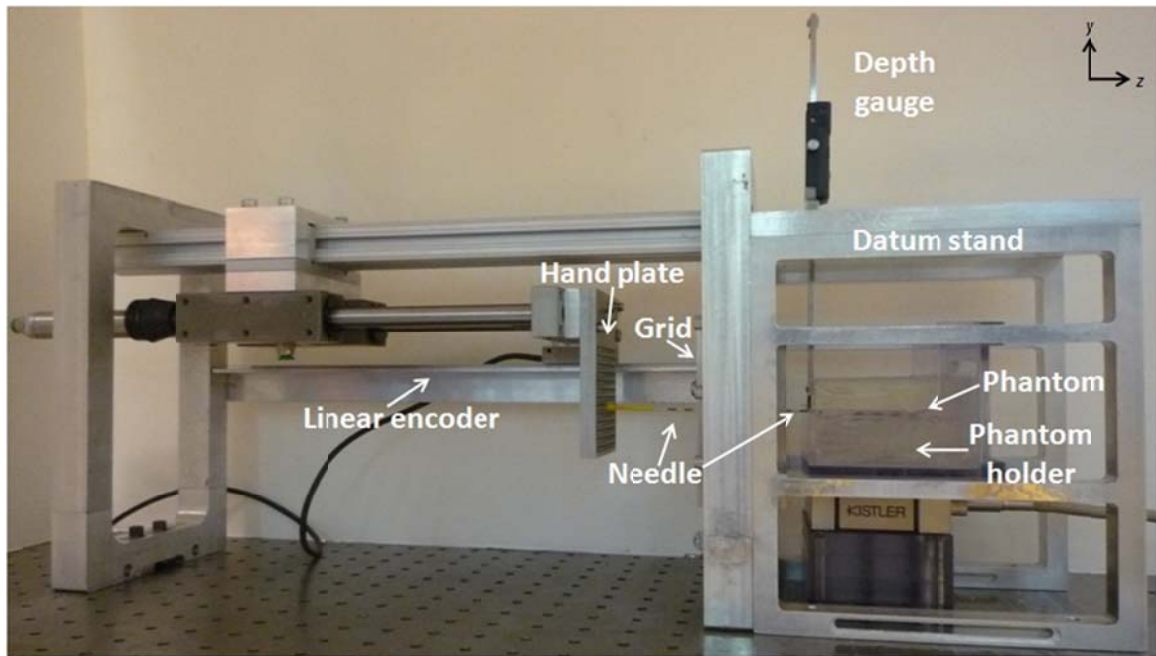
Figure 2.4. Experimental set-up which displays the linear encoder and hand plate used to measure the position of the needle during hand insertion. Needle insertion speed was calculated from displacement and time data.

2.2.2 Procedure for Gauge Repeatability and Reproducibility (GR&R)

GR&R was performed on the datum stand by the procedure outlined by Stamatis [24]. This procedure requires 10 trials, the same three operators measuring each trial, each operator measuring each trial three times, with each trial consisting of four position measurements (X_{enter}, X_{exit}, Y_{enter}, and Y_{exit}). For the GR&R, an operator performed the test as follows: one needle was inserted through the grid, very slowly by hand and into the phantom. The operator obtained position coordinates of the needle in the order of X_{enter} and X_{exit} for the x-direction and Y_{enter} and Y_{exit} for the y-direction and recorded the values for Measurement #1 data. After completing and documenting the data on the first set of measurements, the operator re-measured the needle for

position coordinates two more times. Three operators independently executed the measurements on the same inserted needle, performing the same measurement procedure as outlined. After the first needle insertion was performed, 9 more insertion trials using a different hole in the grid were made, for a total of 10 needle insertion trials, and similar measurements were performed on the needle by the three operators. Analysis to the data was performed as outlined by Stamatis [24].

2.2.3 Design of Experiments

2.2.3.1 Factors and conditions

A 2^k factorial design experiment [27], where $k = 3$ (factors) at two levels or values, was performed in this study. In a factorial design, all possible combinations of factor levels are tested. As shown in Table 2.2, the three factors were needle speed, grid thickness, and grid tightness. The 2^3 factorial design experiment produced eight condition combinations, each having 10 replicates for a total of 80 data points for the entire experiment. A sample size of $n = 10$ was obtained using the operating characteristic (OC) curve and the respective sample size equation [27], discussed in Appendix A. Because of the extensive time required to measure the needle position coordinates along with randomizing the order of the replicates and grids, the experiment was performed over two days, with four conditions executed in one day. In Table 2.2, the first column identifies the eight conditions used in experimentation while the next three columns state the factor level at the respective condition. The last few columns show which conditions are studied: main effects (the overall effect of one factor), two-way interaction (the effect of one factor depending on the level of the second factor – total of two factors simultaneously), and three-way interaction (the effect of two factors depending on the level of the third factor – total of three factors simultaneously). Conditions shown in Table 2.2 were arranged so that the three main effects and the three-way interaction, between factors were performed on day 2, while the other four conditions would be performed on day 1.

Table 2.2. Design matrix of condition combinations including day assignment

| Test #: Conditions studied | Factors | | | Main effect | Interactions | | Day |
	Needle Speed	Grid Thickness	Grid Tightness		Two-way	Three-way	
1: Control	slow	thin	loose				1
2: Speed	fast	thin	loose	X			2
3: Thickness	slow	thick	loose	X			2
4: Speed/thickness	fast	thick	loose		X		1
5: Tightness	slow	thin	tight	X			2
6: Speed/tightness	fast	thin	tight		X		1
7: Thickness/tightness	slow	thick	tight		X		1
8: Speed/thickness/tightness	fast	thick	tight			X	2

2.2.3.2 Grid coordinates and alignment

Pilot studies indicated that the starting location of the needle on the grid can influence needle deflection due to deformation of the phantom. In statistics, a Latin square design [27] is a p x p square array containing p rows and p columns and is used to eliminate sources of variability from the row and column factors. To account for any grid effects on the data, a Latin square design was adapted into a "Latin rectangle" because of different number of rows versus columns. This "Latin rectangle" will enable grid hole locations to distribute effects equally among the condition combinations. As shown in Fig. 2.5, a 5 x 8 region in the lower central region of the grid was selected to conduct the needle insertions. The region was selected so that repeatable results of each trial could be achieved, as shown in the preliminary tests. The number scheme was developed to confirm that all condition combinations were performed at each row number and column letter; each grid coordinate used only once per day, for each needle insertion. One set of roman numeral represents the ten coordinates needed for the ten replicates for each conditional combination, i.e. all I's in the grid holes are for test #6 (on day 1) and test #3 (on day 2). The region in Fig. 2.5 presents four sets of ten holes to use on one phantom when performing the four condition combinations experiment on one day.

Two phantom blocks, one block per day, were used in this experiment. The phantom block was kept in the same position within the phantom holder and behind the grid. With only one needle insertion occurring per grid coordinate, every needle entered a new area within the phantom. Furthermore, with two adjacent grid holes having 5 mm distance of separation, a needle was always inserted into an unused area within a phantom. As shown by the 5 x 8 grid coordinates (a total of 40 holes) in Fig. 2.5, one insertion occurred into each hole within the grid and phantom, for a total of 80 insertion holes within two phantom blocks over the two day experiment. This experimental design eliminates the mechanical damage created from inserting multiple needles within the same grid coordinates and same needle area of the phantom, thus not affecting needle deflection results later in the experiment.

Preceding each needle insertion, the grid was aligned to the two datum surfaces on the datum stand via measuring a reference needle which was placed through a hole that does not insert into the phantom and adjusting the orientation of the grid to produce a zero deflection on the needle.

2.2.3.3 Full randomization

Randomization was used for the following: (1) assignment of the factors to the coding letters A, B, and C used for analysis purposes; (2) day assignment of the four condition combinations; (3) assignment of the group of ten coordinates to a condition combination that was used for the ten replicates; and (4) the order of the grid coordinates/replicates with the respective grid within the day assignment. Furthermore, a full randomization within each day along with the entire experiment occurred.
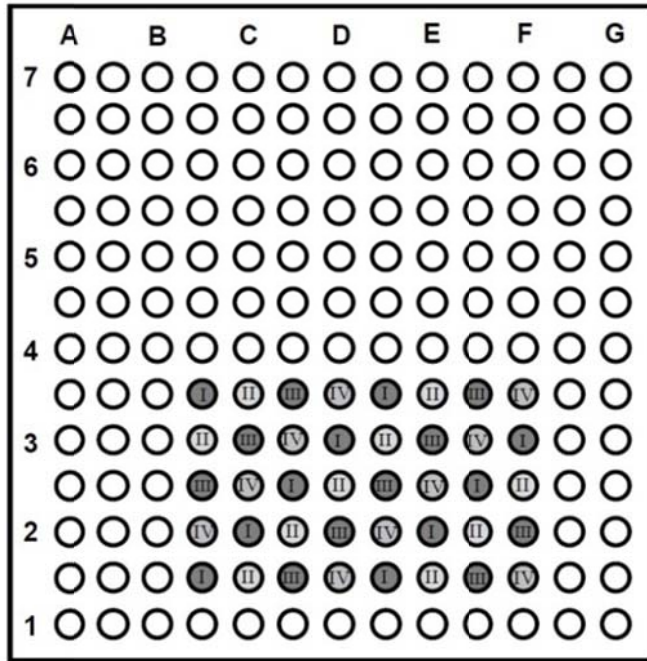
Grid #:	Day 1: Test #	Day 2: Test #
I	6	3
II	4	5
III	1	8
IV	7	2

Figure 2.5. Region of the grid chosen for experiment to distribute effects equally among condition combinations. Roman numerals in the grid correspond to a certain test number, depending on which day the test was performed, as shown in the legend.

2.2.4 Analysis methods

Analyses were performed on the $X_{deflection}$, $Y_{deflection}$, and R data separately. Standard deviation of measured data was used to evaluate the precision and closeness of the replicates to each other within a grid type. Average of the needle deflection data provided an approach to compare accuracy within a grid type. Furthermore, deflection effects were used to analyze the data to provide information on whether any factor(s) had significant effect (p-value < 0.05) on needle deflection. The response variables were all 80 data points collected during the experiment. The $X_{deflection}$, $Y_{deflection}$, and R data were entered as the response variables into the statistical software, Minitab (State College, PA), while speed, thickness, and tightness were used as the two level factors. A 2^3 factorial design ANOVA was performed on the $X_{deflection}$, $Y_{deflection}$, and R data; coded units, -1 for low settings (e.g. all three factor levels for test #1) and $+1$ for high settings (e.g. "fast" needle speed for test #2), was used to define the factor levels. Coded units enable the experimental design to be orthogonal, which allows Minitab to estimate model terms independently. Main effects and two-way interactions were of interest for significant factors. After identifying significant factors, Tukey's test [27] was performed on the highest order terms (significant two-way interactions) in the model to find which means were significantly different from one another.

2.3 RESULTS AND DISCUSSIONS

2.3.1 GR&R Results

Results in Table 2.3 demonstrated that the measurement apparatus developed in this study (Figs. 2.1 and 2.3) is capable to measure the 2 mm needle deflection. GR&R equations utilize a tolerance value in order to calculate the product tolerance used by repeatability error (RPT) within an operator and product tolerance used by reproducibility error (RPD) between operators. Using a tolerance of 2 mm from the target, the RPT, RPD and GR&R for X_{enter}, X_{exit}, Y_{enter}, and Y_{exit} were computed, as shown in Table 2.3.

The 2 mm tolerance was obtained from the radiation oncologist who performs brachytherapy procedures regularly. As shown in Table 2.3, all values of the GR&R were less than 30%. Shina [25] described GR&R as the total variation (due to repeatability and reproducibility error) used to determine if the measurement system is acceptable for its intended applications. A GR&R less than 10% is acceptable and 10% to 30% is marginal acceptable, as it approach 30%, the cut-off value given for an unacceptable system [25]. If the tolerance is reduced to 1 mm, the current measurement apparatus will not be capable for the measurement because the GR&R for X_{enter} and Y_{exit} are both larger than 15%. Furthermore, a 2 mm tolerance is acceptable for measuring needle deflection.

Table 2.3. GR&R results for X_{enter}, X_{exit}, Y_{enter}, and Y_{exit}

Error	X_{enter}	X_{exit}	Y_{enter}	Y_{exit}
RPT	12.5%	10.5%	6.1%	12.8%
RPD	3.9%	1.2%	2.9%	2.3%
GR&R	16.4%	11.7%	9.0%	15.1%

2.3.2 Average and standard deviation of needle deflection

Using Grubbs' test [28,29], discussed in Appendix A, one of the replicates from the tight thin grid with fast insertion was tested as an outlier. This replicate's Z value was 2.33, greater than the critical values of 2.29 (for $n = 10$), thus that data was removed from the study. The measured $X_{deflection}$ and $Y_{deflection}$ for the remaining 79 tests are plotted in Fig. 2.6.

Analysis was performed on 79 data points for $X_{deflection}$, $Y_{deflection}$, and R to obtain the average and standard deviation of the needle deflection and results are summarized in Table 2.4. The average represents the accuracy of the needle insertion while the standard deviation represents the precision.

Initial observation of Fig. 2.6 shows large upward $Y_{deflection}$ data when compared to the $X_{deflection}$ data. The upward shift in $Y_{deflection}$ could be explained by the dynamics of the

phantom during fast insertions. The top surface of the phantom was left unsecure to avoid placing any force on the phantom, thus as the needle inserts into the phantom the top of the phantom bends backward. As the needle moves through the phantom, the phantom readjusts to its original position (the top returning forward), causing the needle to increase in an upward $Y_{deflection}$, as shown in Fig. 2.7. This phenomenon might have led to higher $Y_{deflection}$ values. However, because the "Latin rectangle" design of experiment enable all condition combinations to be tested at each row number and column letter within the grid, an equal distribution of needle insertion into the grid coordinates occurred for all condition combinations.

In Table 2.4, average of the needle deflection provides accuracy of the insertion while standard deviation provides precision and closeness of the replicates to each other. The effect of grid tightness, grid thickness, and the needle speed are discussed:

(i) Tightness: In all 12 cases for $X_{deflection}$, $Y_{deflection}$, and R in Table 2.4, tight grids decrease the average of the needle deflection, when comparison occurred between grids of the same thickness and speed. As far as standard deviation, a tight grid does not necessary decrease standard deviation. At fast insertion speed, the needle is hard to control during insertion thus an increase in variation is observed. At slow insertion speed, the tight thick grid has the smallest standard deviation for the $X_{deflection}$, $Y_{deflection}$, and R data.

(ii) Thickness: Thickness alone does not have a dominant effect on the average and standard deviation of needle deflection. Our current experimental set-up does not improve the average and standard deviation of the needle deflection when a thicker grid was used.

(iii) Speed: Inserting the needle at slow speed reduces both the averages and standard deviation of the needle deflection for most conditions. Only two exceptions for the $X_{deflection}$ data - the loose thin grid for average needle deflection and the tight thin grid for standard deviation - are observed having a slightly higher $X_{deflection}$ value when inserting the needle at slow speed. The $Y_{deflection}$ and R data for all 16 cases (8 cases for average and 8

cases for standard deviation) are consistently lower with slow needle insertion speed. One explanation is that the operator has a steady control of the needle during the slow insertion to reach the consistent target each time. However, there are differences between the experimental set-up and what occurs in the operating room for prostate brachytherapy in which high speed hand needle insertion is commonly applied [30]. The homogeneous phantom in this study versus the heterogeneous skin, muscle, prostate and prostate tumor in brachytherapy is the most significant difference [31]. Additionally, after insertion into the body, the needle deforms and displaces the prostate and thus deviates from its intended path; known as the splay and roll effect by radiation oncologist, slow insertion speed of the needle to produce small deflection may not be applicable to the clinical procedures because of this effect [32].

The overall smallest average and standard deviation occurs when using the tight thin grid and the tight thick grid at slow speed. This supports the conclusion that tight grids and slow needle speed reduces the needle deflection.

Improvements on precision and decrease needle deflection can be seen on the $X_{deflection}$ and $Y_{deflection}$ data points when the tight thick grid [Fig. 2.6(d)] was used during slow insertion. Furthermore, at fast insertion speed, which is the approach commonly used in current brachytherapy procedure, the tight thin and tight thick grids produced more data points that were closer to the target (0, 0) and within the 2 mm circle, when compared to the loose thin and loose thick grids. Overall, the grid tightness (tighter clearance hole) is important to decreasing the needle deflection.
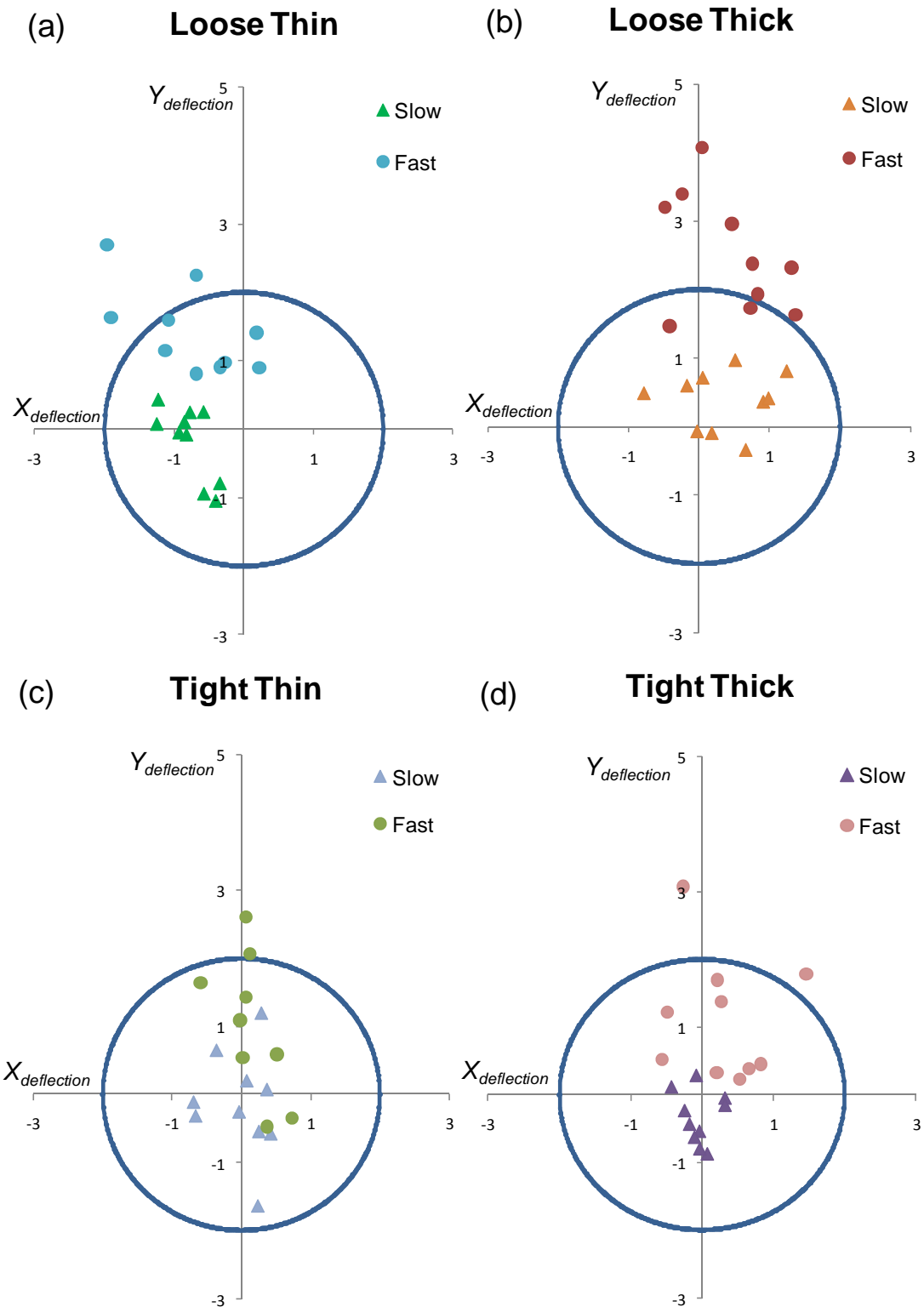
Figure 2.6. $X_{deflection}$ and $Y_{deflection}$ data points (in mm) for slow and fast needle insertion using the (a) loose thin, (b) loose thick, (c) tight thin, and (d) tight thick grids. A 2 mm circle is drawn in order to have a means of visualizing how many and how far data points were from target (0,0).

Table 2.4. Average and standard deviation* of needle deflection for all four grids

Speed	Grid	Average			Standard deviation		
		$X_{deflection}$ (mm)	$Y_{deflection}$ (mm)	R (mm)	$X_{deflection}$ (mm)	$Y_{deflection}$ (mm)	R (mm)
Slow	Loose thin	-0.77	-0.18	0.97	0.31	0.54	0.21
	Loose thick	0.36	0.38	0.79	0.62	0.43	0.42
	Tight thin	-0.01	-0.14	0.72	0.42	0.77	0.44
	Tight thick	-0.04	-0.33	0.51	0.24	0.39	0.20
Fast	Loose thin	-0.76	1.43	1.71	0.76	0.63	0.81
	Loose thick	0.44	2.51	2.65	0.68	0.87	0.78
	Tight thin	0.14	1.02	1.30	0.37	1.04	0.72
	Tight thick	0.29	1.11	1.32	0.62	0.91	0.85

*0.01 mm resolution for measurement tool
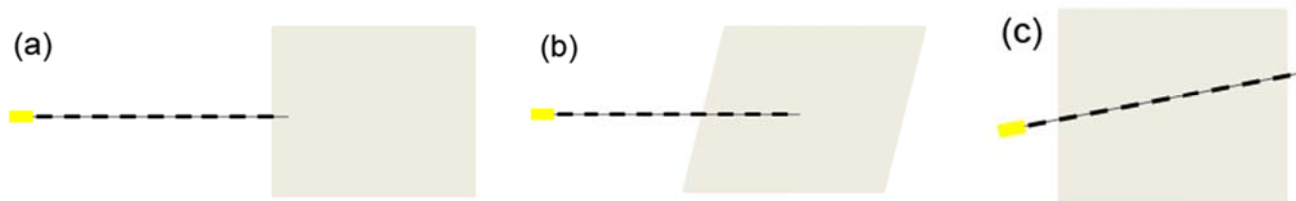
Figure 2.7. Large upward Ydeflection data occurs after (a) needle enters phantom, (b) top of phantom deforms as needle penetrates, then (c) phantom un-deforms and pushes needle up as it returns to the original position.

2.3.3 Deflection significant factors

2.3.3.1 Significant factors for $X_{deflection}$, $Y_{deflection}$, and R deflection data

ANOVA analysis is used to make simultaneous comparison between two or more means; thus the p-values indicate if there are differences between levels of a factor (main effects) and if differences of one factor depends on the level of other factor(s) (two-way and three-way interactions) [27]. Table 2.5 shows the *p*-value with significant (*p*-value < 0.05) marked by bold for the main effect, two-way interaction, and three-way interaction of $X_{deflection}$, $Y_{deflection}$, and R. Significant main effects and two-way interaction included the thickness, tightness, and thickness/tightness for $X_{deflection}$; the speed, thickness, tightness, and thickness/tightness for $Y_{deflection}$; and the speed, tightness, speed/tightness, and speed/thickness for R. One observation that stands out in Table 2.5 is that tightness was significant for all data types ($X_{deflection}$, $Y_{deflection}$, and R), thus it is an important factor to consider when decreasing needle deflection. Furthermore, all three-way interactions demonstrated (*p*-value > 0.05) that the difference observed has only a 5% probability of not being random, thus performing the assigned condition combination on a certain day did not likely affect the significant outcome of the main effect and two-way interaction.

2.3.3.2 Multiple comparisons for significant $X_{deflection}$, $Y_{deflection}$, and R deflection data

With the thickness/tightness two-way interaction having a significant *p*-value for both the $X_{deflection}$ and $Y_{deflection}$ data, along with speed/thickness and speed/tightness for the R data, Tukey's test [27] was performed to find which averages were significantly different from one another within the two-way interaction. Tukey's test, based on a studentized range distribution q, compares all possible pairs of means within the respective two-way interaction. Of the six possible differences in mean for $X_{deflection}$, only

a subset was calculated to be significant. Similar results hold for the $Y_{deflection}$ and R data, as shown in Tables 2.6 and 2.7.

For $X_{deflection}$ in Table 2.6, the loose thin grid (Pair II) has significant differences (difference = Pair I − Pair II) to the other three grids, as shown by the loose thin grid having a p-value = 0.000 (p-value < 0.05) when compared to the other three grids. Furthermore, the loose thin grid had a larger average deflection (for $X_{deflection}$ data) than the other tightness/thickness combinations (or other grids) in Pair I (see Table 2.4). Consequently, the loose thin combination was the worst grid to obtain small $X_{deflection}$. By similar analysis for $Y_{deflection}$, two grids - the loose thin and loose thick grids (Pair II) – showed significant differences with grids in Pair I, consisting mostly of tight grids; thus the loose grids should not be used to obtain small $Y_{deflection}$.

The results for Tukey's test on the speed/tightness interactions from the R data, shown in Table 2.7, revealed significant differences mostly between loose grids in Pair II and tight grids in Pair I, with each tightness type present in three out of four comparisons. With regards to the speed/thickness interactions, most of the thin grids (Pair II – thickness), were shown to have a significant difference with most of the thick grids (Pair I – thickness). The average deflection values for R, shown in Table 2.4, demonstrate relative higher deflections in the Pair I group of speed/thickness (mainly fast and thick) compared to the Pair II group (mainly slow and thin). The results strongly support the claim that loose grids and fast speed are the worse conditions to obtain lower R.

Collectively, these results again prove the benefits for using the tight grid. Furthermore, significant improvements were made on decreasing the needle deflection during needle insertion as shown by the number of significant p-value less than 0.05 when the factor tightness was a main effect or within a two-way interaction.

Table 2.5. p values (< 0.05 are bolded) for $X_{deflection}$, $Y_{deflection}$, and R data

Factor(s)	$X_{deflection}$	$Y_{deflection}$	R
		p-value	
Tightness	**0.024**	**0.000**	**0.000**
Thickness	**0.000**	**0.021**	0.297
Speed	0.247	**0.000**	**0.000**
Thickness/tightness	**0.000**	**0.009**	0.084
Speed/thickness	0.619	0.228	**0.015**
Speed/tightness	0.427	0.082	**0.030**
Speed/thickness/tightness	0.834	0.720	0.115

Table 2.6. $X_{deflection}$ and $Y_{deflection}$ Tukey's test for significant tightness/thickness two-way interactions

Data type	Pair I Tightness	Pair I Thickness	Pair II Tightness	Pair II Thickness	*p*-value
$X_{deflection}$	Loose	Thick	Loose	Thin	0.000
	Tight	Thin	Loose	Thin	0.000
	Tight	Thick	Loose	Thin	0.000
$Y_{deflection}$	Loose	Thick	Loose	Thin	0.000
	Tight	Thin	Loose	Thick	0.000
	Tight	Thick	Loose	Thick	0.000

Table 2.7. R Tukey's test for significant speed/tightness and speed/thickness two-way interactions

Two-way interaction	Pair I		Pair II		*p*-value
	Speed	Tightness	Speed	Tightness	
Speed/tightness	Fast	Loose	Slow	Loose	0.000
	Slow	Tight	Fast	Loose	0.000
	Fast	Tight	Fast	Loose	0.000
	Fast	Tight	Slow	Tight	0.004
	Speed	Thickness	Speed	Thickness	*p*-value
Speed/thickness	Fast	Thin	Slow	Thin	0.006
	Fast	Thick	Slow	Thin	0.000
	Slow	Thick	Fast	Thin	0.000
	Fast	Thick	Slow	Thick	0.000

2.3.4 Correlation tests

Before accepting the ANOVA results, the $X_{deflection}$, $Y_{deflection}$, and R residual data (observation data minus mean) were verified to be independent (plot of residual versus run order of data), normally distributed (normal probability plot of residual), and show homoscedasticity (plot of residuals versus fitted values) [27]. Using Minitab, abnormal trends did not exist within the data plots. Two correlation tests were performed on the data; the Pearson Correlation test was performed to test deviation magnitudes while the Rayleigh test [33] detected correlation within the direction of the data. Results for the Pearson correlation was 0.086 (p-value = 0.450); since the value was insignificant, the magnitude of the $X_{deflection}$ and $Y_{deflection}$ data are independent. Rayleigh test produced a value of 0.12, which was smaller than the critical value of 0.20; thus, there was no tendency for a particular x- and y- direction to occur together. Furthermore, correlation did not occur within the data.

2.4 CONCLUSIONS

The grid with tight clearance holes demonstrated to be important and advantageous to decrease needle deflection ($X_{deflection}$, $Y_{deflection}$, R). Slow needle insertion speed improved the averages and standard deviation of the needle deflection for all conditions within the $Y_{deflection}$ and R and six out of eight cases within $X_{deflection}$. Likewise, the best results for average and standard deviation of needle deflection occurred with a tight grid at slow insertion speed. Although fast hand needle insertion occurs in current brachytherapy procedures, the tight grid improved the averages and standard deviation of the needle deflection when the needle was inserted at fast speed. Furthermore, statistical analysis showed significant p-values for $X_{deflection}$, $Y_{deflection}$, and R when the grid tightness was the main factor.

Results in this study show the potential to improve needle deflection in current brachytherapy procedures when the tight grid is used. Future work includes using the tight grid to perform fast needle insertion experiments using an imaging modality such as

ultrasound and computed tomography (CT) on the cadaver or animal model to confirm the benefit of needle placement accuracy within the prostate. Even though slow insertion speed proved to be beneficial in our experimental set-up, there are differences between the experimental set-up and what occurs clinically in brachytherapy in which high speed hand needle insertion is commonly applied due to the rotation and translation of the prostate. Future work of this research is to investigate the benefit of tight grid for different needle insertion speeds on the cadaver or animal model within the brachytherapy setup.

Additionally, the distance between the grid and phantom can influence needle deflection within the phantom. If the distance the needle travel between the grid and phantom is decreased, smaller needle deflection is possible within the phantom. The effect of distance is a good topic for future study.

REFERENCES

1. S. Nath, Z. Chen, N. Yue, S. Trumpore, and R. Peshcel, "Dosimetric effects of needle divergence in prostate seed implant using ^{125}I and ^{103}Pd radioactive seeds," Medical Physics **27**, 1058-1066 (2000).

2. N. N. Stone and R. G. Stock, "Complications Following Permanent Prostate Brachytherapy," European Urology **41**, 427-433 (2002).

3. J. C. Blasko, T. Mate, J. E. Sylvester, P. D. Grimm, and W. Cavangah, "Brachytherapy for Carcinoma of the Prostate: Techniques, Patient Selection, and Clinical Outcomes," Seminars in Radiation Oncology **12,** 81-94 (2002).

4. A. T. Porter, J. C. Blasko, P. D. Grimm, S. M. Reddy, and H. Ragde, "Brachytherapy for Prostate Cancer," CA: A Cancer Journal for Clinicians **45**, 165-178 (1995).

5. J. Shan, N. Hata, and R. Kikinis, "Needle insertion simulation for image-guided brachytherapy of prostate cancer," *2nd International Conference on Bioinformatics and Biomedical Engineering* (Shanghai, China, 2008), pp. 1682–1685.

6. S. P. DiMaio and S. E. Salcudean "Needle insertion modeling and simulation," IEEE Transactions on Robotics and Automation **19**, 864–875 (2003).

7. D. Glozman and M. Shoham, "Flexible needle steering and optimal trajectory planning for percutaneous therapies," *Proceedings of the 7th International Conference on Medical Image Computing and Computer-Assisted Intervention – MICCAI* (Saint-Malo, France, 2004), pp. 137-144.

8. T. K. Podder, D. P. Clark, J. Sherman, D. Fuller, E. Messing, D. Rubens, J. Strang, R. Brasacchio, L. Liao, W. S. Ng, and Y. Yu, "*In vivo* motion and force measurement of surgical needle intervention during prostate brachytherapy," Medical Physics **33**, 2915-2922 (2006).

9. N. Abolhassani, R. V. Patel, and F. Farzam, "Minimization of needle deflection in robot-assisted percutaneous therapy," The International Journal of Medical Robotics and Computer Assisted Surgery **3**, 140-148 (2007).

10. H. Kataoka, T.Washio, M. Audette, and K. Mizuhara, "A Model for relations between needle deflection, force, and thickness on needle penetration," *Proceedings of the 4th*

International Conference on Medical Image Computing and Computer-Assisted Intervention, (Utrecht, The Netherlands, 2001), pp. 966–974.

11. N. Abolhassani, R. Patel, and F. Ayazi, "Effects of different insertion methods on reducing needle deflection," *29th Annual International Conference of the IEEE Engineering in Medicine and Biology Society*, (Lyon, France, 2007), pp. 491–494.

12. H. Kataoka, T. Washio, K. Chinzei, K. Mizuhara, C. Simone, and A. M. Okamura, "Measurement of the tip and friction force acting on a needle during penetration," *Proceedings of the 5th International Conference on Medical Image Computing and Computer-Assisted Intervention* — MICCAI (Tokyo, Japan, 2002), pp. 216-223.

13. A. M. Okamura, C. Simone, and M. D. O'Leary, "Force modeling for needle insertion into soft tissue," IEEE Transactions on Biomedical Engineering **51** pp. 1707-1716 (2004).

14. G. Wan, Z. Wei, L. Gardi, D.B. Downey, and A. Fenster, "Brachytherapy needle deflection evaluation and correction," Medical Physics **32**, 902-909 (2005).

15. M. A. Meltsner, N. J. Ferrier, and B.R. Thomadsen, "Observations on rotating needle insertions using a brachytherapy robot," Physics in Medicine and Biology **52**, 6027-6037 (2007).

16. T. K. Podder, W. S. Ng, and Y. Yu, "Multi-channel robotic system for prostate brachytherapy," *29th Annual International Conference of the IEEE Engineering in Medicine and Biology Society*, (Lyon, France, 2007), pp. 1233–1236.

17. N. Abolhassani, R. Patel, and M. Moallem, "Needle insertion into soft tissue: A survey." Medical Engineering & Physics **29**, 413-431 (2007).

18. F. W. Mick and K. Zabrouski, U. S. Patent No. 6,579,262 (25 January 2000).

19. W. F. Whitmore III, W. E. Barzell, and R. F. Wilson, U. S. Patent No. 6,036,632 (28 May 1998).

20. N. Abolhassani and R. V. Patel, "Deflection of a Flexible Needle during Insertion into Soft Tissue," 28th *Annual International Conference of the IEEE Engineering in Medicine and Biology Society*, (New York City, USA, 2006), pp. 3858 -3861.

21. T. K. Podder, D. P. Clark, J. Sherman, D. Fuller, E. Messing, D. J. Rubens, J. G. Strang, Y. D. Zhang, W. O'Dell, W. S. Ng, and Y. Yu, "Effects of tip geometry of surgical needles: an assessment of force and deflection," *Third European Medical*

and Biological Engineering Conference (Prague, Czech Republic, 2005), pp. 1641-1644.

22. Y. Yu, T. K. Podder, Y. Zhang, W. S. Ng, V. Misic, J. Sherman, L Fu, D. Fuller, E. Messing, D. Rubens, J. Strang, and R. Brasacchio, "Robot-Assisted Prostate Brachytherapy" *Proceedings of the 9th International Conference on Medical Image Computing and Computer-Assisted Intervention* – MICCAI (Copenhagen, Denmark, 2006), pp. 41-49.

23. *Measurement Systems Analysis* (DaimlerChrysler, Ford Motor, and General Motors, 2002).

24. D. H Stamatis, *Six Sigma and Beyond: Statistical Process Control* (St. Lucie Press, Boca Roton, Florida, 2002).

25. S. G. Shina. *Six Sigma Electronics Design and Manufacturing*. (McGraw-Hill, New York, 2002).

26. T. K. Podder, D. P. Clark, D. Fuller, J. Sherman, W. S. Ng, L. Liao, D. Rubens, J. Strang, E. Messing, Y. D. Zhang, and Y. Yu, "Effects of velocity modulation during surgical needle insertion," 27th Annual International Conference of the IEEE Engineering in Medicine and Biology Society, (Shanghai, China, 2005), pp. 5766-5770.

27. D. C. Montgomery, *Design and Analysis of Experiments* (Wiley, New York, 2005).

28. V. Barnett and T. Lewis, *Outliers in Statistical Data* (John Wiley & Sons, New York, 1994).

29. B. Iglewicz and D. C. Hoaglin, *How to Detect and Handle Outliers* (American Society for Quality Control, Wisconsin, 1993).

30. C. S. McGill, J. Schwartz, J. Z. Moore, P. W. McLaughlin, and A. J. Shih, "Effects of insertion speed and trocar stiffness on the accuracy of needle position for brachytherapy" Medical Physics **39**, 1811-1817 (2012).

31. R. Alterovitz, K. Goldberg, J. Pouliot, R. Taschereau, and I-C. Hsu, "Needle Insertion and Radioactive Seed Implantation in Human Tissues: Simulation and Sensitivity Analysis," IEEE International Conference on Robotics & Automation **2**, pp. 1793 – 1799 (2003).

32. P. L. Roberson, V. Narayana, D. L. McShan, R. J. Winfield, and P. W. McLaughlin, "Source placement error for permanent implant of the prostate," Medical Physics **24**, 251-257 (1997).

33. K. V. Mardia, *Statistics of Directional Data* (Academic Press, New York, 1972).

CHAPTER 3

EFFECTS OF INSERTION SPEED AND TROCAR STIFFNESS ON THE ACCURACY OF NEEDLE POSITION FOR BRACHYTHERAPY

ABSTRACT

In prostate brachytherapy, accurate positioning of the needle tip to place radioactive seeds at its target site is critical for successful radiation treatment. During the procedure, needle deflection leads to target misplacement and uneven radiation dose to cancerous cells. In practice, radiation oncologists commonly use high-speed hand needle insertion to minimize displacement of the prostate as well as the needle deflection. Effects of needle insertion speed and stiffness of trocar (a solid rod inside the hollow cannula) on needle deflection are studied. Needle insertion experiments into phantom were performed on a 2^2 factorial design (2 parameters at 2 levels), with each condition having replicates. Analysis of the deflection data included calculating the average, standard deviation, and analysis of variance (ANOVA) to find significant single and two-way interaction factors. The stiffer tungsten carbide trocar is effective in reducing the average and standard deviation of needle deflection. The fast insertion speed together with the stiffer trocar generated the smallest average and standard deviation for needle

deflection for almost all cases. The combination of stiff tungsten carbide trocar and fast needle insertion speed are important to decreasing needle deflection. The knowledge gained from this study can be used to improve the accuracy of needle insertion in the brachytherapy procedure.

3.1 INTRODUCTION

Accurate placement of needles is important when performing multiple medical diagnostic and therapeutic procedures such as anesthesia, neurosurgery, tissue biopsy, and brachytherapy [1-4]. Brachytherapy is a radiation treatment option performed once prostate cancer, the most frequently diagnosed cancer in men [5], is detected in the early stages. When performing brachytherapy, a needle is used to guide radioactive seeds into the prostate gland in order to eradicate cancerous cells [6,7]. The brachytherapy needle consists of two main parts, an inner solid rod called the trocar and an outer hollow cylinder called the cannula. The needle, which is the combination of the cannula and trocar, is inserted into the prostate and deflects due to tissue deformation and complex anatomic structures in and around the prostate [8-10]. Clinical studies have shown that when the needle deflects, the radioactive seed does not attain its target, and consequently the radiation dose deviates from the targeted level [8]. Adverse side effects such as rectal bleeding, urinary and bowel incontinence, erectile dysfunction, and tissue damage occur when the radioactive seeds are misplaced [8-10].

To improve needle insertion accuracy and radioactive seed placement during brachytherapy, studies have been conducted on the needle and needle insertion procedure by exploring different designs of needle tips [11,12], performing different insertion methods [12-16], and modeling needle-tissue interaction [17-19]. Abolhassani et al. [20] has an in-depth survey that includes modeling needle insertion forces and tissue deformation, along with the effect different needle trajectories and paths have on tissue deformation. Additionally, McGill et al. [21] designed a grid (array of holes in block that support the needle prior to entering the tissue) that reduces the clearance between the grid hole inner diameter and the needle outer diameter. Clinically, the 18-gauge needle is the

standard for brachytherapy. A smaller diameter, 20-gauge, needle has recently been tested to reduce the invasiveness. Stiffness of the thin 20-gauge needle is only about 26% of the current 18-gauge needle based on the beam deflection theory. The literature review shows no study has been performed on using a higher Young's modulus material for the trocar to increase the stiffness and reduce the deflection of the needle combination during insertion. One of the goals of this paper is to investigate the effect of trocar stiffness on the needle deflection.

Insertion techniques used to move the needle through the body are important to obtain the desired target within the prostate gland. Currently, manual needle insertions utilizing a quick flick of the wrist to produce high-speed is performed by physicians to achieve the quick and easy penetration of stiffer tissue, such as the perineum skin, during the brachytherapy procedure. Even though the high needle insertion speed does not stay constant during the entire needle path, this instantaneous high-speed has been measured to be around 650 ± 200 mm/s [21]; however, in actual brachytherapy procedure the needle path is non-uniform at the hands of skilled physicians. Mahvash and Dupont [22] concluded from experimenting on pig hearts and modeling it as a viscoelastic material, that increasing needle insertion velocity decreases needle deflection and tissue damage. Researchers have studied speed effects on needle insertion [12-15,23], but the speed range is around 10 mm/s, with a maximum of 200 mm/s when using a robotic-assisted tool [23]. A pneumatic actuator has been applied to generate a faster needle insertion speed (over 2300 mm/s). The pneumatic actuator was chosen over linear motor because of its high-speed capability and clean and cost-effectiveness for clinical applications. A cadaver prostate brachytherapy test using the pneumatic actuator generating such high speeds has been conducted and demonstrated the feasibility of such high-speed in the clinical setting. Another goal of this paper is to study the effect of such fast insertion speed on needle deflection.

This paper begins with the overview of experimental set-up, followed by an introduction to the pneumatic device and trocar material. Next, an explanation of the experimental design and analysis method are presented. Subsequently, results on the average and standard deviation of needle deflection are provided. Significant factors

46

using the deflection data, discussion of the findings, and conclusion of this study are then given.

3.2 MATERIALS AND METHOD

3.2.1 Overview of experimental set-up

The set-up (Fig. 3.1) for the experiment includes a grid, phantom, phantom holder, measurement datum stand, digital depth gauge, pneumatic device (comprise of the pneumatic actuator, linear guide, linear encoder, and needle plate), and needle. The needle grid, made of AISI 316 stainless steel, has a 13 x 13 array of 1.303 mm diameter holes and thickness of 50.8 mm. This grid, which was tested as the tight thick grid in [21], has a 33 μm diametric clearance between the grid hole inside diameter and needle outside diameter, and is 30.5 mm longer than the current commercial 18-gauge grids, which has 76 μm diametric clearance and 20.3 mm length.

The phantom, made of polyvinylchloride (PVC) modified with plastisol, was created from a 1:1 ratio of regular liquid plastic to plastic softener (M-F Manufacturing, TX). An indentation test [24] performed on this PVC phantom of the same ratio produced a Young's modulus of 12 kPa, a value similar to porcine liver [25]; thus the mechanical properties of PVC phantom mimic that of tissue. The phantom block had dimensions of 85 mm length, 75 mm width, and 50 mm height. The 85 mm phantom length was the distance the needle traveled during experimentation. The phantom width-height ratio provided enough support upon the phantom holder and adequate area for needle insertion to occur when using several height levels within the grid.

The phantom holder, made from 12.7 mm thick polycarbonate, was constructed to have 90 mm length, 100 mm width, and 75 mm height, and held the phantom as in [21]. The phantom holder provided a consistent location to obtain needle position. The phantom holder and phantom were placed 25 mm from the front of the needle grid. This distance mimics the gap found between the patient's skin and grid during brachytherapy procedures.

The measurement datum stand and digital depth gauge (Mitutoyo Model VDS-6 DCX) are the components that comprised the needle deflection measurement apparatus discussed in [21]. Using the datum stand, the depth gauge mechanically measures position coordinates at the phantom entrance and exit in the x- and y- directions, perpendicular to the needle axial direction. Using the position coordinates, the $X_{deflection}$ and $Y_{deflection}$, the needle deflection in the horizontal and vertical direction, respectively, were calculated. Additionally the resultant/radial deflection R ($= \sqrt{X_{deflection}^2 + Y_{deflection}^2}$) data were calculated through the 85 mm phantom length [21].

The descriptions on the pneumatic device and the needles with the stiffer trocar used in this experiment are explained in the following Sections 3.2.1.1 Pneumatic device and 3.2.1.2 Needle stiffness, respectively.
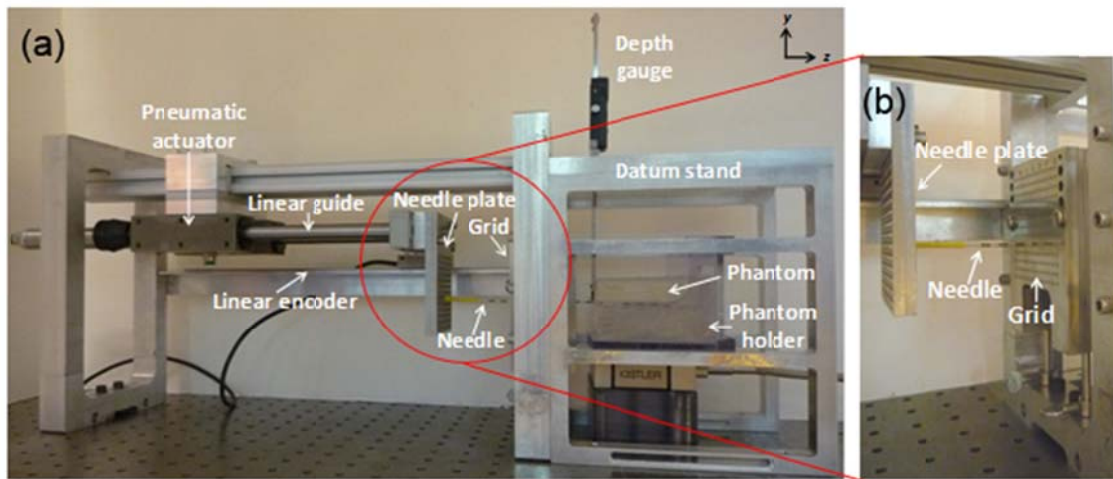
Figure 3.1. (a) Experimental set-up which includes the grid, phantom, phantom holder, measurement datum stand, digital depth gauge, pneumatic device (pneumatic actuator, linear guide, linear encoder, and needle plate), and needle and (b) close-up view of the needle plate, needle, and grid.

3.2.1.1 Pneumatic device

This device, shown in Fig. 3.1, uses a pneumatic actuator with a 19 mm bore 150 mm stroke (Numatics Model SG-543136-1) to move the linear guide and push the attached needle plate. Within the pneumatic actuator casing are linear bearings that enable the linear guide to move forward and backward in the *z*-direction. Rubber stoppers, placed at the end of the linear guide, were used to control the stoke length, thus guarantee a constant needle depth for each insertion trial. The needle plate, having the same 13 x 13 array of holes as the grid, pushed the needle through the grid and into the phantom. The holes within the needle plate provide a means to enclose the back of the needle and thus push the needle through the grid, when the actuator is activated. The speed of the pneumatic actuator was controlled by varying the inlet air pressure to the actuator.

3.2.1.2 Needle stiffness

Mick Radio-Nuclear Instruments Inc. (NY, USA) produces 18-gauge prostate brachytherapy needles (Model MTP-1820-C) that were used in this experiment. The needle consists of two main parts made of AISI 304 stainless steel: the inner solid trocar rod and the outer hollow cannula. The trocar has a diamond point (three-plane) while the cannula tip has square cut. The needle combination (trocar and cannula) must resist various deflecting forces exerted on the needle during insertion into tissues. A mechanical property that indicates stiffness of a material is called Young's modulus or modulus of elasticity. The Young's modulus of the current trocar made of AISI 304 stainless steel (SS) is about 200 GPa [26]. To increase the stiffness of the needle combination, the tungsten carbide with 6% cobalt, denoted as WC, with a Young's modulus of around 630 GPa [27], was used as the material for the solid trocar. This WC trocar has the same tip angle (10.5° angle), diameter (1.01 mm), and length (20.5 cm) as the current Mick AISI 304 stainless steel trocar (Fig. 3.2) and can be inserted into the current hollow AISI 304 stainless steel cannula.

49

Figure 3.2. Trocars made of (a) AISI 304 stainless steel and (b) tungsten carbide in 6% cobalt.

3.2.1.3 Needle insertion set-up and speed

During the experiment, the needle was set to the insertion position by placing the needle tip within a hole in the grid (trocar orientation was random relative to the bevel cuts at the trocar's tip), while the other end was placed within the matching hole in the needle plate. The matching hole within the needle plate enabled the needle to be parallel with the optical table, which is the base of the experimental setup. After placing the needle tip within the grid (the same starting position and orientation for all insertions for a given grid coordinate), the air valve was set to the desired air pressure. The device was secured to the optical table to prevent movement during insertion. The linear optical encoder (Fig. 3.1) measured the position of the needle plate during insertion. A data acquisition system (National Instruments Model NI DAQPad-6015) and LabVIEW, sampling rate of 50 kHz, was used to record the data. Using the displacement and time data, the insertion speed produced by the pneumatic device was calculated. Air flow at 140 kPa produced speed of 1120 ± 40 mm/s, while air flow at 410 kPa produced speed at 2370 ± 30 mm/s. These two speeds represent the low limit and close to the highest speed of the pneumatic actuator. After the needle was inserted into the phantom, position coordinates were obtained at the entrance and exit of the phantom to calculate needle deflection ($X_{deflection}$ and $Y_{deflection}$). Measurements were repeated for each insertion. The needle tip cutting edges were examined after each test and no visible wear was observed for both stainless steel and tungsten carbide trocar.

3.2.2 Design of Experiments

3.2.2.1 Factors and conditions

A 2^k factorial design experiment [28], where $k = 2$ (factors), was executed in this study. The two factors were needle insertion speed and material used for the trocar, as shown in Table 3.1. Using the 2^2 factorial design experiment, four condition combinations were produced. Each combination had ten replicates producing a total of 40 data points for the entire experiment. The sample size ($n = 10$) was calculated using an operating characteristic (OC) curve and appropriate sample size equation, which was presented in [21]. In Table 3.1, the first column shows the four conditions studied in this experiment while the next two columns state the factor level for the needle speed and material used for the trocar (stainless steel - SS and tungsten carbide - WC) at the respective condition. The last two columns identify the main effect (the overall effect of one factor) and two-way interaction (the effect of one factor depending on the level of the second factor) which are represented by the test # and condition.

Table 3.1. Design matrix of condition combinations

Test #: Conditions studied	Factors		Main Effect	Two-way Interaction
	Needle Speed (mm/s)	Trocar Material		
1: Control	1120	SS		
2: Speed	2370	SS	X	
3: Material	1120	WC	X	
4: Speed/Material	2370	WC		X

3.2.2.2 Grid coordinates, alignment, and randomization

A 5 x 8 section (row by column) in the lower region of the grid was used to perform all 40 needle insertion trials. Ten coordinates, which represented the ten

replicates, were assigned to one condition combination. Using the "Latin rectangle" design for grid coordinates for each condition and replicate, discussed in [21], all condition combinations were performed at each row number and column letter, for each needle insertion.

Before beginning the experiment, the grid was aligned to the two datum surfaces on the datum stand via inserting by hand and measuring a reference needle which was placed through a hole that does not insert into the phantom. Adjustment was made to the orientation of the grid to produce a zero deflection on the needle. Additionally, a full randomization occurred throughout the entire experiment via: (1) assignment of the ten grid coordinates (as shown in [21]) to a condition combination that was used for the ten replicates; (2) order of grid coordinates/replicates; and (3) assignment of factors to two coding letters, used for analysis purposes.

3.2.3 Analysis methods

Each data set ($X_{deflection}$, $Y_{deflection}$, and R) were analyzed separately; analysis included average, standard deviation, and p-values. Averages provided a method to compare accuracy of needle insertion while standard deviations compare precision and closeness of replicates with each other within each condition. Using the needle deflection effects to analyze the data, p-values were used to show which factor(s) had a significant (p-value < 0.05) effect on needle deflection. A 2^2 factorial design analysis of variance (ANOVA) was performed on the $X_{deflection}$, $Y_{deflection}$, and R data, using the statistical software Minitab (State College, PA). All 40 data points from the experiment were used as the response variables for the $X_{deflection}$, $Y_{deflection}$, and R data, while the needle speed and trocar material were entered as the two-level factors within Minitab. Coded units, -1 for low settings (e.g., both factor levels for test #1) and $+1$ for high settings (e.g., both factor levels for test #4), were used to define the factor levels. Coded units enable the experimental design to be orthogonal, thus Minitab is able to estimate model terms independently.

3.3 RESULTS AND DISCUSSIONS

3.3.1 Average and standard deviation of needle deflection

All 40 $X_{deflection}$ and $Y_{deflection}$ data points are plotted in Fig. 3.3. Using Grubbs' test [29,30], data points within each condition did not deviate from the other points/replicates, thus outliers were not detected within any condition. All 40 data points for $X_{deflection}$, $Y_{deflection}$, and R were analyzed to obtain the average and standard deviation of the needle deflection; results are summarized in Table 3.2 and Fig. 3.4. The average represents accuracy of needle insertion while the standard deviation represents the precision and closeness of replicates to each other.

Taking the average of all the $X_{deflection}$ data revealed a 0.60 mm shift to the right, while the $Y_{deflection}$ data produced a slight shift of 0.01 mm in the up direction. The shift in the data is possible because the needle and needle grid, which were calibrated via a slow hand needle insertion, did not have the same calibration as a needle inserted with the faster speed produced by the pneumatic device. To resolve the difference in calibration, a readjustment occurred by shifting the $X_{deflection}$ data 0.60 mm to the left. Since the $Y_{deflection}$ data shift was small, those data points were not altered. The $X_{deflection}$ data was investigated and verified that a common effect occurred within all factor combination. The original and shifted data results including standard deviation, average (minus the shift), and statistics were the same for both data set. Furthermore, adjustment of the $X_{deflection}$ data occurred by shifting the data to obtain a new average $X_{deflection}$ data close to 0, which is a similar value as the raw $Y_{deflection}$ data.

Initial observation of Fig. 3.3 displays needle deflection mainly in the $Y_{deflection}$ data, when compared to the $X_{deflection}$ data. Bias is present within the $Y_{deflection}$ data for all parameters studied because of the boundary conditions of the phantom. The top of the phantom is exposed while the entire bottom and 50% of both sides (x-directional deflection) of the phantom are constrained via the phantom holder (Fig. 3.1). Additionally, there is a bias in the positive y-direction [Fig. 3.3(a)] for the 2370 mm/s (higher speed) because higher speeds produce higher forces. Higher force produces

higher needle deflection when the less stiff trocar (stainless steel) is used compared to the stiffer tungsten carbide trocar [Fig. 3.3(b)].

In Table 3.2, the average of the needle deflection provides accuracy of the insertion while standard deviation provides precision and closeness of the replicates to each other. The effects of trocar material and needle insertion speed are discussed:

(i)   Trocar material: In 5 out of the 6 cases for $X_{deflection}$, $Y_{deflection}$, and R data (in Table 3.2), the higher Young's modulus WC trocar material decrease the average of the needle deflection, for a given insertion speed. The only exception was the $Y_{deflection}$ data at 1120 mm/s insertion speed. For standard deviation, 4 out of the 6 cases showed a decrease in standard deviation, with an additional one case staying the same, when the WC material was used during needle insertion. The only exception (R data at 1120 mm/s insertion speed) observed to having a slightly higher standard deviation value, an increase of 0.06 mm, when using the WC trocar during needle insertion. One explanation for this finding is that the stiffness of the trocar plays a more dominate role at faster needle insertion speeds, as shown with the 6 out of 6 cases decreasing (with one case staying the same) the average and standard deviation of the needle deflection when the WC and faster needle insertion speed (2370 mm/s) was used.

(ii)   Needle speed: Inserting the needle at the faster speed (2370 mm/s) reduces the average needle deflection for 4 out of the 6 cases for the $X_{deflection}$, $Y_{deflection}$, and R data, for a given trocar material. Only two exceptions, the WC for the $X_{deflection}$ data, which produced a small increase of 0.06 mm, and SS for the $Y_{deflection}$ data; both have a higher value when inserting the needle at the faster speed. For standard deviation of needle deflection, both cases of the $Y_{deflection}$ data values and one of each of the $X_{deflection}$ and R data are reduced (total of 4 out of 6 cases), when a speed of 2370 mm/s was used. The two exceptions, SS for the R data which increased by a value of 0.05 mm and WC for the $X_{deflection}$ data, did not

54

decrease the standard deviation value when inserted at the faster speed. One explanation is that the faster speed of 2370 mm/s usually overcomes the tissue deformation better during insertion than the slower speed, thus the faster inserted needle is able to produce consistent accurate and precise needle insertion.

Figure 3.4 summarizes the R needle deflection findings shown in Table 3.2, illustrating the WC material inserted at the faster speed of 2370 mm/s produced the least amount of average R deflection and the least amount of standard deviation in R. The WC trocar material inserted at the faster speed (2370 mm/s) also improved the $X_{deflection}$ and $Y_{deflection}$ averages and standard deviations for almost all (10 out of 12) cases in Table 3.2, which includes one case staying the same, for the $X_{deflection}$, $Y_{deflection}$, and R results when compared to the WC trocar inserted at the slower speed (1120 mm/s) and SS trocar inserted at the faster speed (2370 mm/s).

The positive attributes of WC and faster speed are also illustrated by visual comparison in Fig. 3.3(b), that shows more replicates of the WC inserted at a speed of 2370 mm/s are within or closer to the 0.5 mm radius circle. This supports the conclusion that WC and the faster insertion speed (2370 mm/s) improve needle position accuracy and consistency.
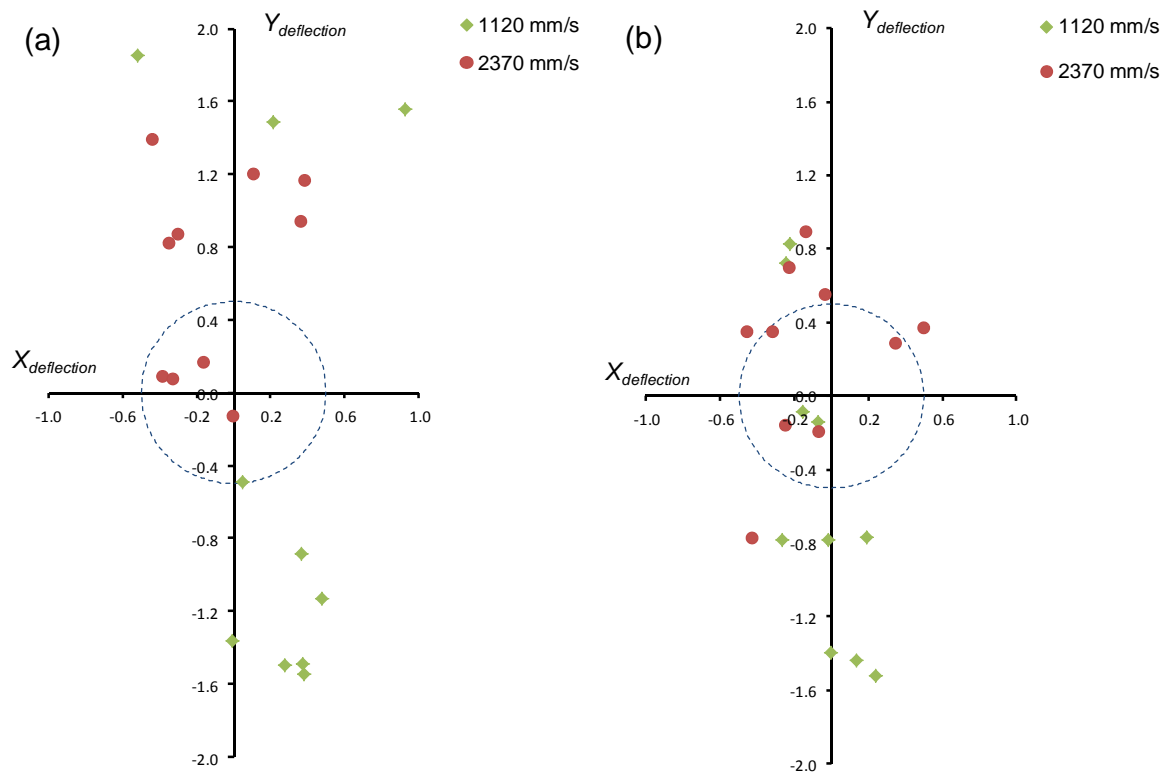
Figure 3.3. X_deflection and Y_deflection data points (in mm) at speeds of 1120 mm/s and 2370 mm/s using a trocar made of (a) SS and (b) WC. A 0.5 mm circle is drawn in order to have a means of visualizing how many and how far data points were from the target (0,0).

Table 3.2. Average and standard deviation of needle deflection

Needle speed (mm/s)	Trocar material	Average			Standard deviation		
		$X_{deflection}$ (mm)	$Y_{deflection}$ (mm)	R (mm)	$X_{deflection}$ (mm)	$Y_{deflection}$ (mm)	R (mm)
1120	SS	0.25	-0.35	1.39	0.37	1.41	0.42
	WC	-0.04	-0.54	0.87	0.18	0.85	0.48
2370	SS	-0.11	0.66	0.78	0.31	0.55	0.47
	WC	-0.10	0.24	0.57	0.31	0.49	0.23
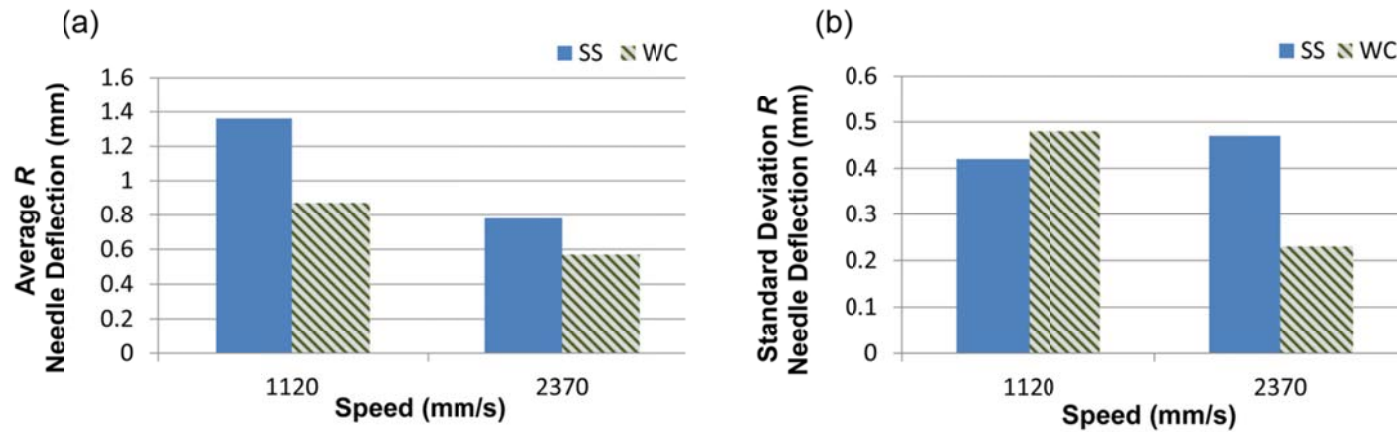
Figure 3.4. R data: (a) average and (b) standard deviation of needle deflection of SS and WC trocar material inserted at 1120 mm/s and 2370 mm/s.

3.3.2 Deflection significant factors

Table 3.3 provides the *p*-value for the main effect and two-way interactions of $X_{deflection}$, $Y_{deflection}$, and R data, with significant (*p*-value < 0.05) marked in bold. Significant main effects included the needle speed for $X_{deflection}$, needle speed for $Y_{deflection}$, and needle speed and trocar material for R. One observation to mention in Table 3.3 is that the needle speed factor was significant for all data types ($X_{deflection}$, $Y_{deflection}$, and R); thus the needle speed, with the contribution of trocar material (being significant with R data), are both important to decreasing the needle deflection.

Table 3.3. *p* values (< 0.05 are bolded) for $X_{deflection}$, $Y_{deflection}$, and R data

Factor(s)	*p*-value		
	$X_{deflection}$	$Y_{deflection}$	R
Needle speed	**0.034**	**0.004**	**0.001**
Trocar material	0.134	0.296	**0.008**
Speed/material	0.128	0.682	0.239

3.3.3 Correlation tests

Before performing the ANOVA tests, $X_{deflection}$, $Y_{deflection}$, and R residual data (observation data minus mean) were confirmed to be independent (plot of residual versus time order of data collection), normally distributed (normal probability plot of residual), and show homoscedasticity (plot of residuals versus fitted data) [28]. Abnormal trends did not exist within the data plot when Minitab was used. Additionally, correlation tests were performed to test deviation magnitudes on the absolute value of the data, using the Pearson Correlation test, and correlation within the direction of the data using the Rayleigh test [31]. Results from the Pearson correlation was 0.266 (*p*-value = 0.098), while Rayleigh test produced a value of 0.12, which was smaller than the critical value of 0.27. Both results were insignificant and less than the critical value, respectively; thus

correlation did not occur within the data. Therefore, the magnitude of the absolute $X_{deflection}$ and $Y_{deflection}$ data and the x- and y- direction of the data are both independent.

3.4 CONCLUSIONS

This experiment produced results that show the importance of inserting a stiffer trocar at speeds much faster than what can be produced by hand insertion or current robotic devices that are in literature. The WC trocar material inserted at faster speed (2370 mm/s) produced less average needle deflection and lower average standard deviation of needle deflection than the SS trocar material inserted at slower speed (1120 mm/s) for each of the R data. The WC trocar inserted at the faster speed (2370 mm/s) produced the smallest results for average and standard deviation for each of the $Y_{deflection}$ and R data. Furthermore, statistical analysis showed significant p-values for $X_{deflection}$, $Y_{deflection}$, and R data for the speed factor and R data for the material factor.

This research discovers the optimal combination of trocar material and insertion speed. The optimal insertion speed to minimize the needle deflection is not investigated. Such optimal needle speed, which depends on the setup condition and phantom, does exist and is a good topic for future study. A few limitations of this study include using a homogenous phantom instead of the heterogeneous tissue and experimenting with only two pneumatic insertion speeds. The phantom provided a consistent specimen to perform repeated needle insertion in order to confirm decreased needle deflection. The observed effect of decreasing deflection with higher insertion speeds produced by the pneumatic device could contribute to improve targeting of the needle when inserting through the prostate tissue. Additionally, another limitation consists of calibrating the needle grid to the pneumatic device. This could be a potential source of bias, even though correlation tests were performed on the data to identify bias within the result. Although this experimental design has few factors for an idealized set-up, new concepts and materials are introduced and its findings can be of interest for future investigation. Future work of this research includes studying the optimal needle speed to minimize needle deflection in phantom test and investigating the feasibility of the high-speed needle obtaining more

accurate targeted positions in a mobile and deformable phantom, which represents the prostate. Additionally, the pneumatic device and WC trocar will be used to experiment on cadaver and animal models to confirm accurate needle insertion within a prostate.

REFERENCES

1. J. Moore, C. Clarke, D. Bainbridge, C. Wedlake, A. Wiles, D. Pace, and T. Peters, "Image Guidance for Spinal Facet Injections Using Tracked Ultrasound," *Proceedings of the 12th International Conference on Medical Image Computing and Computer-Assisted Intervention* – MICCAI (London, England, 2009), pp. 516-223.

2. H. Xu, A. Lasso, S. Vikal, P. Guion, A. Krieger, A. Kaushal, L. L. Whitcomb, and G. Fichtinger, "MRI-Guided Robotic Prostate Biopsy: A Clinical Accuracy Validation," *Proceedings of the 13th International Conference on Medical Image Computing and Computer-Assisted Intervention* – MICCAI (Beijing, China, 2010), pp. 383-391.

3. R. R. Shamir, L. Joskowicz, and Y. Shoshan, "Optimal landmarks selection and fiducial marker placement for minimal target registration error in image-guided neurosurgery," Proceedings of SPIE – Medical Imaging **7261**, 72612N-1 - 72612N-8 (2009).

4. S. Song, N. B. Cho, G. Fischer, N. Hata, C. Tempany, G. Fichtinger, and I. Iordachita, "Development of a Pneumatic Robot for MRI-guided Transperineal Prostate Biopsy and Brachytherapy: New Approaches," *IEEE International Conference on Robotics and Automation*, (Anchorage, Alaska, 2010), pp. 2580-2585.

5. American Cancer Society, "*Cancer facts and figures 2011*," Atlanta, GA, American Cancer Society, 2011.

6. A. T. Porter, J. C. Blasko, P. D. Grimm, S. M. Reddy, and H. Ragde, "Brachytherapy for Prostate Cancer," CA: A Cancer Journal for Clinicians **45**, 165-178 (1995).

7. J. C. Blasko, "Brachytherapy," Urology **55**, 306-308 (2000).

8. S. Nath, Z. Chen, N. Yue, S. Trumpore, and R. Peshcel, "Dosimetric effects of needle divergence in prostate seed implant using ^{125}I and ^{103}Pd radioactive seeds," Medical Physics **27**, 1058-1066 (2000).

9. N. N. Stone and R. G. Stock, "Complications Following Permanent Prostate Brachytherapy," European Urology **41**, 427-433 (2002).

10. J. C. Blasko, T. Mate, J. E. Sylvester, P. D. Grimm, and W. Cavangah, "Brachytherapy for Carcinoma of the Prostate: Techniques, Patient Selection, and Clinical Outcomes," Seminars in Radiation Oncology **12,** 81-94 (2002).

11. T. K. Podder, D. P. Clark, J. Sherman, D. Fuller, E. Messing, D. J. Rubens, J. G. Strang, Y. D. Zhang, W. O'Dell, W. S. Ng, and Y. Yu, "Effects of tip geometry of surgical needles: an assessment of force and deflection," *Third European Medical and Biological Engineering Conference* (Prague, Czech Republic, 2005), pp. 1641-1644.

12. M. A. Meltsner, N. J. Ferrier, and B.R. Thomadsen, "Observations on rotating needle insertions using a brachytherapy robot," Physics in Medicine and Biology **52**, 6027-6037 (2007).

13. N. Abolhassani, R. Patel, and F. Ayazi, "Effects of different insertion methods on reducing needle deflection," *29th Annual International Conference of the IEEE Engineering in Medicine and Biology Society*, (Lyon, France, 2007), pp. 491-494.

14. T. K. Podder, W. S. Ng, and Y. Yu, "Multi-channel robotic system for prostate brachytherapy," *29th Annual International Conference of the IEEE Engineering in Medicine and Biology Society*, (Lyon, France, 2007), pp. 1233-1236.

15. K. Yan, W. S. Ng, K. V. Ling, T. Liu, Y. Yu, and T. K. Podder, "High frequency translational oscillation & rotational drilling of the needle in reducing target movement," *IEEE International Symposium on Computational Intelligence in Robotics and Automation*, (Espoo, Finland, 2005), pp. 163-168.

16. G. Wan, Z. Wei, L. Gardi, D.B. Downey, and A. Fenster, "Brachytherapy needle deflection evaluation and correction," Medical Physics **32**, 902-909 (2005).

17. S. Jiang, N. Hata, and R. Kikinis, "Needle insertion simulation for image-guided brachytherapy of prostate cancer," *2nd International Conference on Bioinformatics and Biomedical Engineering*, (Shanghai, China, 2008), pp. 1682-1685.

18. S. P. DiMaio and S. E. Salcudean, "Needle insertion modeling and simulation," IEEE Transactions on Robotics and Automation, **19**, pp. 864-875 (2003).

19. D. Glozman and M. Shoham, "Flexible needle steering and optimal trajectory planning for percutaneous therapies," *Proceedings of the 7th International Conference on Medical Image Computing and Computer-Assisted Intervention – MICCAI* (Saint-Malo, France, 2004), pp. 137-144.

20. N. Abolhassani, R. Patel, and M. Moallem, "Needle insertion into soft tissue: A survey." Medical Engineering & Physics **29**, 413-431 (2007).

21. C. S. McGill, J. A. Schwartz, J. Z. Moore, P. W. McLaughlin, and A. J. Shih, "Precision grid and hand motion for accurate needle insertion in brachythearpy," Medical Physics **38**, 4749-4759 (2011).

22. M. Mahvash and P. E. Dupont, "Fast Needle Insertion to Minimize Tissue Deformation and Damage," *IEEE International Conference on Robotics and Automation*, (Kobe, Japan, 2009), pp 3097-3102.

23. T. K. Podder, D. P. Clark, D. Fuller, J. Sherman, W. S. Ng, L. Liao, D. J. Rubens, J. G. Strang, E. M. Messing, Y. D. Zhang, and Y. Yu, "Effects of velocity modulation during surgical needle insertion," *27th Annual International Conference of the IEEE Engineering in Medicine and Biology Society*, (Shanghai, China, 2005), pp. 5766-5770.

24. V. Egorov, S. Tsyuryupa, S. Kanilo, M. Kogit, A. Sarvazyan, "Soft tissue elastometer," Medical Engineering & Physics **30**, 206-212 (2008).

25. L. Gao, Q. Zhang, M. Liu, "Indentation test of soft tissue for investigating needle tissue machining," *2nd International Conference of Mechanic Automation and Control Engineering* (MACE), (Hohhot, China, 2011), pp. 348-351.

26. American Society for Metals, *ASM handbook Vol. 6: Welding, Brazing, and Soldering* (ASM International, Ohio, 1993).

27. American Society for Metals, *ASM handbook Vol. 2: Properties and Selection: Nonferrous Alloys and Special-Purpose Materials* (ASM International, Ohio, 1990).

28. D. C. Montgomery, *Design and Analysis of Experiments* (Wiley, New York, 2005).

29. V. Barnett and T. Lewis, *Outliers in Statistical Data* (John Wiley & Sons, New York, 1994).

30. B. Iglewicz and D. C. Hoaglin, *How to Detect and Handle Outliers* (American Society for Quality Control, Wisconsin, 1993).

31. K. V. Mardia, *Statistics of Directional Data* (Academic Press, New York, 1972).

CHAPTER 4

FORCE DISTRIBUTION AND PREDICTION OF NEEDLE DEFLECTION IN TISSUE INSERTION

ABSTRACT

The distribution of axial and normal forces during needle insertion are experimentally measured as inputs for finite element analysis (FEA) models to predict the needle deflection and phantom deformation for accurate needle tip placement. Obtaining the target location is essential for many needle-based procedures which deliver treatment to or extract samples from the body. In this study, the 18-gauge hollow cannula with a solid trocar tip is inserted into the phantom while simultaneously measuring the force via dynamometer and the needle deflection and phantom deflection via the non-contact magnetic sensor. The assumption of a triangular-shape normal force distribution during needle insertion is validated experimentally. The cutting, friction, and normal forces are extracted from measured forces and used as inputs on FEA models. The FEA predicted needle deflection and phantom deformation are reasonably accurate compared with magnetic tracking measurements. The knowledge gained from this study can be implemented on manual or robotic needle devices in which forces versus insertion distance are measured for compensation in order to achieve the desired trajectory and the target.

4.1 INTRODUCTION

Percutaneous needle insertion into soft tissues is one of the common methods used to deliver therapy for treatment or extract the tissue or blood sample for diagnosis. Accurate positioning of the needle tip to the specific target is important to the success of medical procedures, particularly in brachytherapy, anesthesia, and biopsy [1-3]. For example, in brachytherapy, a radiation treatment commonly used for prostate cancer, the radioactive seed location within the cancerous cells and the efficacy of treatment greatly depends on the accuracy of the needle tip placement [5,6]. Inaccurate needle placement occurs because of the soft and inhomogeneous tissue properties which results in tissue deformation, anatomical obstruction around the prostate, and limited maneuverability during needle insertion [6-8].

During needle insertion, the needle-tissue interaction influences the force distribution and deflection of the needle. The fracture mechanics and rupture deformation were used to model the crack extensions in studies of the *ex vivo* porcine liver skin and *in vivo* human skin while examining the energy and work that occurs during needle insertion into tissue [9-13]. Researchers have identified the axial force for needle insertion in *in vitro* liver tissue [14,15], *ex vivo* canine's prostate [16], two-layer turkey muscle [17], and the polyvinylchloride (PVC) phantom tissue [18] experiments. The distribution of normal force (perpendicular to the insertion direction) on the needle has been described in the literature [19-21]. However, the experimental validation of the normal force distribution was not shown. Personal discussion with the corresponding author (Abolhassani) confirms that the stated normal force distribution in [19-21] was an assumption. The normal force on the needle surface during insertion is important because it affects the needle deflection and tip placement, i.e., accuracy of needle tip position, during insertion within the tissue. One of the goals of this research is to experimentally validate the assumption of the needle normal force distribution during insertion into tissue.

To study the needle-tissue interaction, researchers had modeled the needle as a cantilever beam to calculate needle deflection [19-24] and presented the tissue forces on the needle as the virtual spring support [24-27]. An in-depth survey by Mirsa et al. [28]

presented a variety of methods which attempted to model needle-tissue interactions using the linear and nonlinear elasticity based finite element method with the Voigt mass-spring-damper model. In another survey, Abolhassani et al. [29] presented modeling of the needle insertion forces and effects different insertion techniques (such as robotic insertion and needle rotation) and trajectories had on the needle placement and tissue deformation. Many of these studies independently focused on needle steering or tissue deformation. A few investigators attempted to measure needle deflection and phantom deformation simultaneously [30-32]. An one degree-of-freedom load sensor measured the needle axial force while the tissue deformation was estimated from the motion sensor and algorithm [30]. Crouch et al. [31] stated that needle trajectory and phantom deformation occurred, however results for the needle path and model were not presented. Likewise, a study by Haddadi et al. [32] measured needle and phantom relative movement during experimentation; however the phantom deformation path and model were not shown throughout the needle insertion path. Another goal of this paper is to explore a new approach to measure both the needle deflection and phantom deformation using the non-contact magnetic tracking sensor while simultaneously acquiring three-directional needle-tissue interaction forces. The measured forces will be the input for finite element analysis (FEA) models used to predict the needle deflection and phantom deformation, which will be compared with experimental measurements.

A variety of techniques have been used to measure the needle deflection and tissue deformation during experimentation. Researchers have used biplane x-ray [33] and graph papers on each sides of a phantom block in the needle insertion direction [34,35] to measure needle deflection within the tissue material. Abolhassani et al. [19-21] used the magnetic tracking which includes a five degree-of-freedom sensor coil that was placed within the needle tip, in order to track the needle position during insertion. To measure the tissue deformation, fiducial markers have been placed within the phantom, while periodically capturing images during needle insertion to track the marker (and tissue) displacement [31]. McGill et al. [36,37] has developed a precision x-y datum platform to measure the needle position and deflection during insertion into the phantom and studied effects of precision grid, stiff trocar material, and high insertion speed. The final goal of

this paper is to develop a FEA model by using the measured forces to predict the needle deflection and tissue deformation.

The paper begins with the concept of the force model for the needle deflection and tissue deformation, in addition to an explanation of the FEA models. The overview of the experimental setup and validating the force model are then presented, followed by the description of the magnetic tracking which measures the needle and phantom position. Next, a summary is provided on how to obtain and analyze the force and sensor data for both needle deflection and phantom deformation. Results of the experimentally measured forces, needle deflection, and phantom deformation and comparison with FEA predictions are shown, followed by the discussion on the validation of the FEA models.

4.2 FORCE MODELS FOR NEEDLE INSERTION

During needle insertion into tissue, the needle-tissue interaction produces forces which result in needle deflection and tissue deformation. To predict the relative motion between the needle and tissue, a force model is presented, Fig. 4.1, which identifies the axial (x-directional) and normal (z-directional) forces during needle insertion. The axial force F_x consists of cutting force (F_c) and friction force (F_f). Their relationship is shown in Equation 4.1.

$$F_x = F_c + F_f \tag{4.1}$$

The F_c breaks the tissue, thus it remains almost constant for the duration of the needle insertion under the assumption of homogenous material properties. The F_f increases with time as the contact area between tissue and the needle increases over time. Assuming the unit-length friction force, f_f, the F_f is

$$F_f = f_f L \tag{4.2}$$

where L is the distance of needle insertion to the phantom.

The normal force (F_z) is produced by the pressure from the surrounding tissue during the needle insertion and it portrays a specific distribution along the needle $f_z(x)$, thus

$$F_z = \int_0^L f_z(x)\, dx \qquad (4.3)$$

In this study, the f_z is hypothesized as a triangular distribution with the peak portion near the needle entrance side and is proven experimentally in Section 4.3.
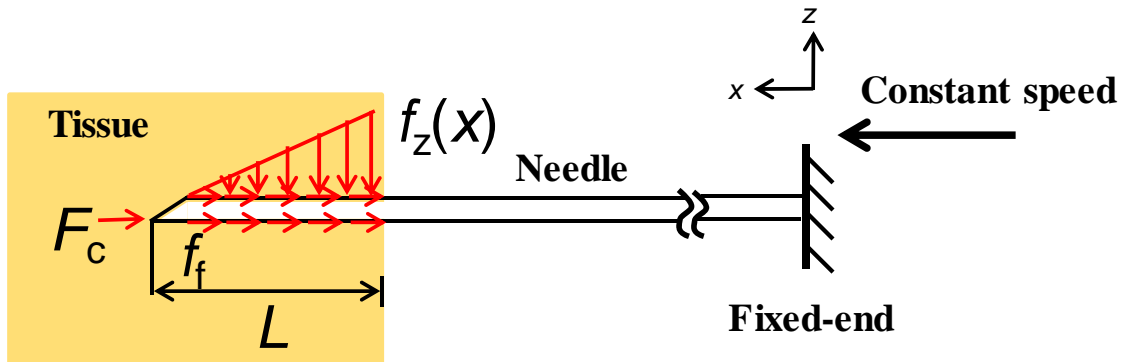
Figure 4.1. Force model of needle-tissue interaction with the axial (*x*-directional) forces - cutting force (F_c) and friction force (f_f) - and normal (*z*-directional) force (f_z) shown in arrows. Needle shown as cantilever beam with fixed-end support and L presenting the distance of needle insertion within the tissue

The needle deflection and tissue deformation are calculated using FEA. Since forces are given (inputs) in this study, it is not necessary to utilize contact and material failure functions of FEA. Instead, the needle and tissue models can be decoupled and modeled separately. The needle (Fig. 4.1), shown as a cantilever beam with fixed-end support, has both the axial and normal forces placed near the tip, where phantom penetration occurs. Using ABAQUS/CAE FEA software (Simulia; Paris, France), a needle model was created to apply all three forces (F_c, F_f, and F_z) to obtain the needle

deflection, as shown in Fig. 4.2(a). FEA was chosen over the cantilever beam equation because the axial force (F_c and F_f) could contribute to the needle bending, especially in large needle deflection. In FEA, the needle was simplified to a long tube (no bevel) with the cutting force evenly distributed, denoted as f_c, at the bottom half of the circular needle tip to mimic its effect on the needle deflection. The resultant of f_c equals to F_c. The friction force (f_f) was evenly distributed along the needle surface. The normal force was applied as a resultant normal force F_z in the z-direction at its respective distance according to the triangular-shape normal force distribution.

For the FEA of phantom, Figure 4.2(b) shows the mesh with a needle hole of length L. Within the hole surface, the f_c and f_f are applied. The effect of f_z is expected small on the phantom deformation and can be neglected. For the small needle deflection case in this study, the needle hole is assumed to be straight. Similar to the needle FEA, f_f was evenly distributed within the inner hole circumference and f_c was distributed evenly at the phantom hole wall. Boundary conditions, to be elaborated in Section 4.3.4.3, are applied based on the tissue securing method.

(a)

(b)
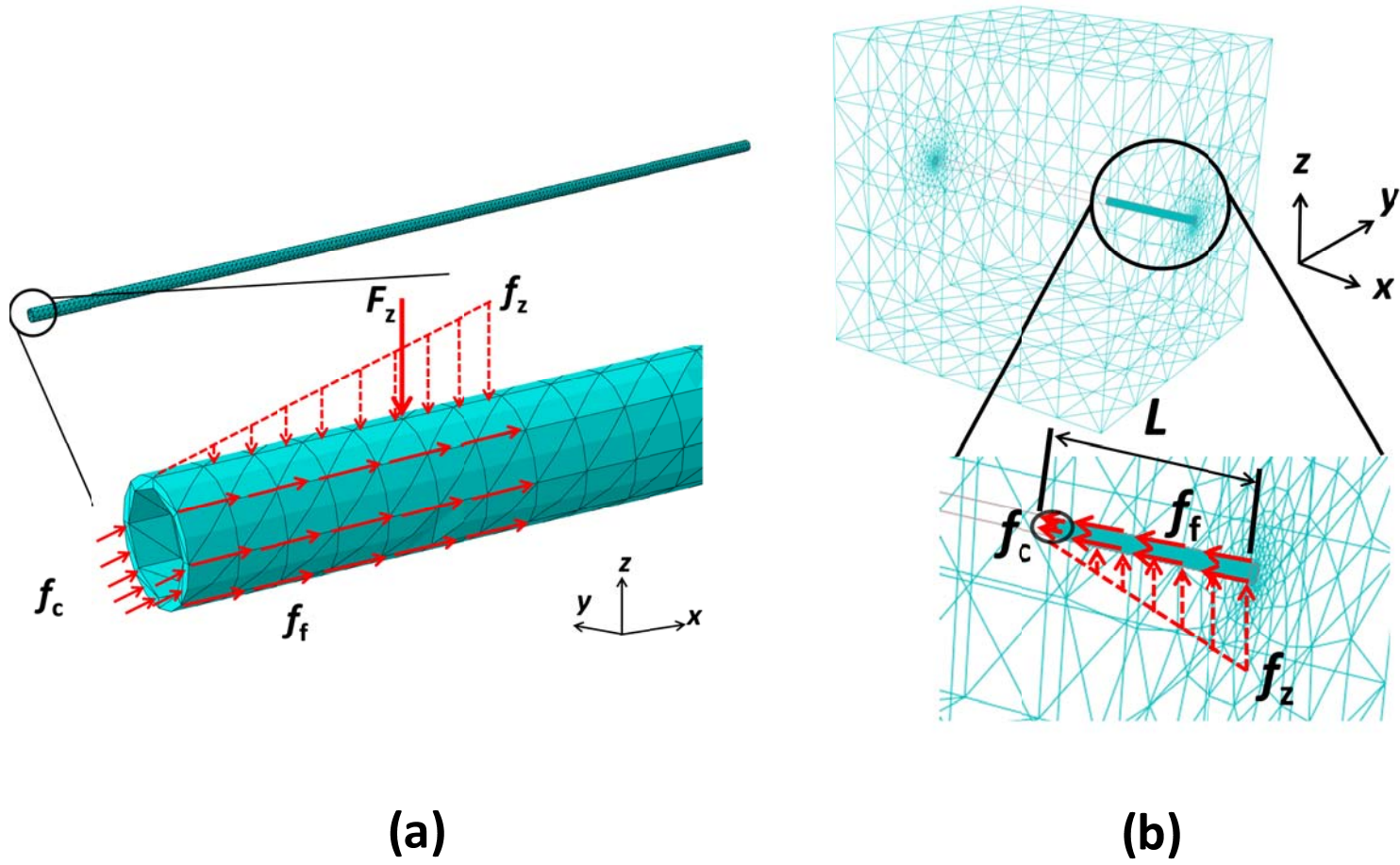
Figure 4.2. FEA (a) needle and (b) phantom models.

4.3 MATERIALS AND METHOD

4.3.1 Overview of experimental setup

The setup (Fig. 4.3) for the experiment includes the needle, needle holder, linear stages, phantom tissue, phantom holder, and force dynamometer. The needles used were the 18- gauge prostate brachytherapy needles (Model MTP-1820-C, Mick Radio-Nuclear Instruments Inc., New York, USA) which are often used in the clinical brachytherapy procedure. The brachytherapy needle consisted of a solid 1.01 mm diameter trocar and a hollow 1.27 mm outer diameter cannula, both made of stainless steel. A 30º bevel angle was generated at the tip via grinding the trocar and cannula together using a grinding wheel within a grinding machine (Chevalier Smart 919, California, USA). To obtain a hollow needle with a solid tip for the placement of a 0.9 mm diameter miniature magnetic sensor (described in Section 4.3.2) at the cannula tip for tracking, a 5 mm (from the top of the bevel angle) length trocar tip was cut and permanently glued to the hollow cannula. The placement of the trocar and cannula bevel angles was confirmed to be in the same position as when they were initially grinded together. The aluminum needle holder, with a 1.3 mm diameter, 15 mm deep hole proximal to the phantom, held the needle tightly via a screw, which when tighten, secured the needle. A constant needle length of 90 mm protruding from the holder was confirmed for each set of experimental test. Three Siskiyou Instrument (Grants Pass, Oregon), Model 200cri and 100cri, linear stages with 10 μm resolution are the actuators which provided the linear motion at a constant speed of 1.5 mm/s.

Phantom was adopted as the tissue-mimicking material which was made of PVC modified with plastisol, and was created from a 1:1 ratio of regular liquid plastic to plastic softener (M-F Manufacturing, Texas). This is a phantom material that commonly used in needle insertion tests [36,37]. The Young's modulus of this phantom is around 18 kPa, similar to porcine liver. The phantom block was created to 50 mm in length (in the same direction of the needle insertion), 50 mm in width, and 50 mm in height. The phantom holder, constructed from 12.7 mm thick polycarbonate, was 60 mm in length, 75

71

mm in width, and 75 mm in height. The phantom holder constrained the entire bottom and 50% of both sides of the phantom; an opening (40 mm in width and 35 mm in height) at the back of the phantom holder allowed the needle to protrude out of the phantom after full insertion. The piezoelectric force dynamometer (Kistler Model 9256A1, Winterthur, Switzerland) was placed beneath the phantom holder to acquire three directional force data when the needle is inserted into the phantom.
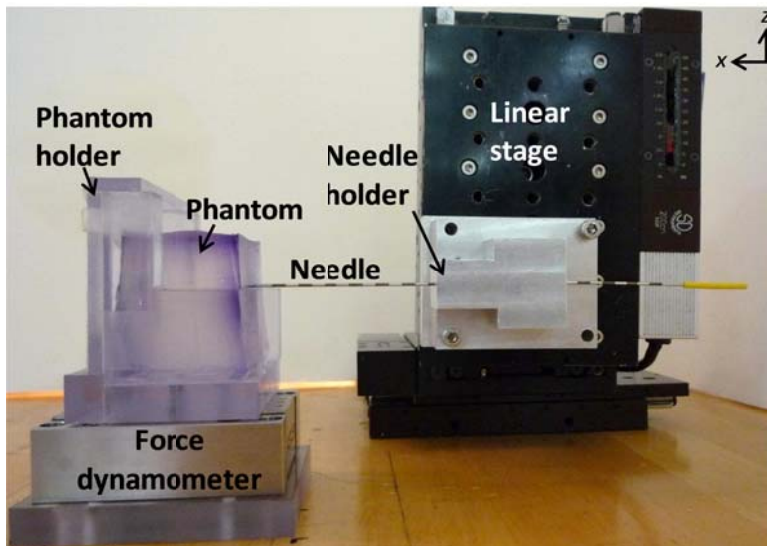
Figure 4.3. Experimental set-up including the needle, needle holder, linear stages, phantom, phantom holder, and force dynamometer.

4.3.2 3D magnetic non-contact position sensor

The 3D magnetic non-contact position tracking system, TrackSTAR Model 90 by Ascension Technology Corporation (Milton, Vermont, USA), was used to measure the needle and phantom positions during experimentation. This system, as shown in Fig. 4.4, consists of a miniature six degree-of-freedom sensor with 0.9 mm outer diameter and 7.25 mm length, a transmitter with 360 mm range, and the TrackSTAR electronic unit to convert the sensor signal to positions and orientations. The electro-magnetic transmitter creates the magnetic field by direct current (DC) pulses. Three orthogonal coils within

72

the transmitter are sequentially pulsed at 50 Hz frequency. The sensors pick up the electromagnetic field and relay the information back to the electronic unit, which calculates three positions in x-, y-, and z-direction as well as three orientations (roll, elevation, and azimuth angles, respectively) of the sensor. Figure 4.4 demonstrates the three translational and three rotational directions, reference from the transmitter, while displaying the entire experimental set-up which includes the linear stages, needle (with sensor within the hollow cannula tip and compared to a penny), phantom, phantom holder, force dynamometer, and 3D magnetic tracking system. To decrease the magnetic interference, the entire experimental set-up was position and secured on a wood table. In order to test the sensor's dynamic accuracy, a test was performed to obtain the average and standard deviation stepping motion values (see Appendix B) and to identify the optimal location of the transmitter relative to the needle for best accuracy of position tracking. Results showed that when the sensor is pointed at the front side of the transmitter (marked in Fig. 4.4), this configuration produced the most accurate measurement results.

Figure 4.4. Experimental set-up with includes the 3D Guidance TrackSTAR Model 90 (transmitter, electronic unit, and sensor within the hollow cannula tip and compared to a penny), linear stages, needle, phantom, phantom holder, and force dynamometer.
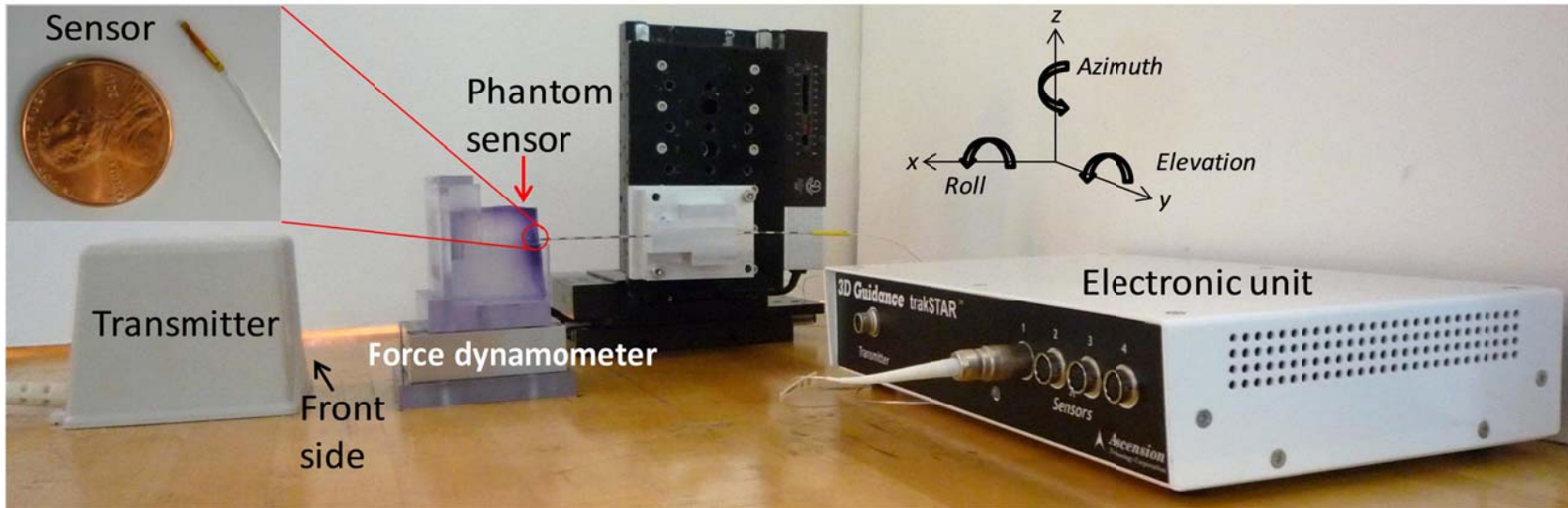
4.3.3 Experimental procedures

Using the experimental set-up presented in Figs. 4.3 and 4.4, two miniature sensors were used to measure the needle deflection and phantom deformation during the needle-tissue insertion experimentation. One sensor was placed 5 mm from the tip inside the 18- gauge cannula with the 5 mm trocar tip. In order to minimize the sensor movement within the hollow cannula, the cable which connects the sensor to the TrackSTAR electronic unit was secured at the distal end of the needle. The second sensor was placed on the top middle surface of the phantom, near the needle insertion face, shown as the phantom sensor in Fig. 4.4. The transmitter, with the Front Side facing the sensors, was placed in front of the needle. The needle with 30º bevel down orientation is secured by the needle holder and driven by the actuator to insert into the phantom.

Before the needle-phantom insertion test, the phantom was first removed and the needle was inserted 50 mm into air with the sensor acquiring deflection data for the 50 mm travel distance to generate the datum for deflection calculation. Next, the phantom was placed into the holder and the linear stage inserted the needle 50 mm into the phantom, while both needle deflection and phantom deformation data were measured at 70 Hz sampling rate by magnetic tracking and the F_x and F_z were attained via the force dynamometer, recording the data at a sampling rate of 1.5 kHz via a data acquisition system (National Instruments Model NI DAQPad-6015) and LabVIEW.

To separate the F_f and F_c from F_x, an additional insertion was performed after the initial needle- phantom insertion. After inserting the needle into the phantom, the needle was retracted until the very tip of the needle remained in the phantom. The needle was re-inserted 50 mm via the x-directional linear stage into the same location within the phantom as the previous insertion, while acquiring the force data. Since the needle tends to follow the path of least resistance, the needle travelled the same path as the previous insertion. Thus, only the F_f was recorded within the second insertion in the axial direction.

4.3.4 Analysis methods

4.3.4.1 F_f and F_c

In order to decompose the F_x (after needle tip penetration) into F_c and F_f, one repeated needle insertion was performed. After the needle tip penetrates and travels through new sections of the tissue, cutting occurs via the needle tip and F_f is present between the needle body and tissue (Fig. 4.1). Researchers have separated F_c and F_f using: (1) a load cell where one-axis acquired the F_c and the other axes obtained the F_x, then the F_c was subtracted from the F_x to obtain the F_f [16] and (2) an initial needle insertion occurred into a specimen to obtain the F_x, followed by continuing insertion and/or reversing the direction of insertion without cutting new tissue [14,15]. The force acquired without cutting new tissue (continuous forward insertion and/or retraction) is F_f. This is the approach adopted in this study.

Our experimental design obtains the F_c from the F_x by subtracted the F_x of the second needle insertion from the F_x of the first needle insertion. The axial force was decomposed to cutting and friction forces and both were applied to the phantom model, at their respective location [Fig. 4.2(b)], to predict the deformation.

4.3.4.2 Triangular-shape normal force distribution

Assuming that the axial force F_x has limited effect, the needle deflection can be expressed by the cantilever beam equation,

$$\delta = \frac{F_z l^2}{6EI}(2l + 3b) \tag{4.4}$$

and Fig. 4.5 where F_z is the resultant normal force, δ is the needle deflection at the insertion depth, b is the distance between the location of F_z and needle tip, l is the length from F_z to fixed-end support, E is the Young's modulus of stainless steel needle, and I is

the area moment of inertia of stainless steel hollow cannula of the needle. Since the triangular distribution of normal force was hypothesized in this study, F_z should fall at the position where b equals to $0.667L$. To prove this hypothesis, an analysis method has been developed to find the ratio of b to L, denoted as R, at each depth during the needle insertion based on the experimentally measured δ and F_z and given L, E, and I.
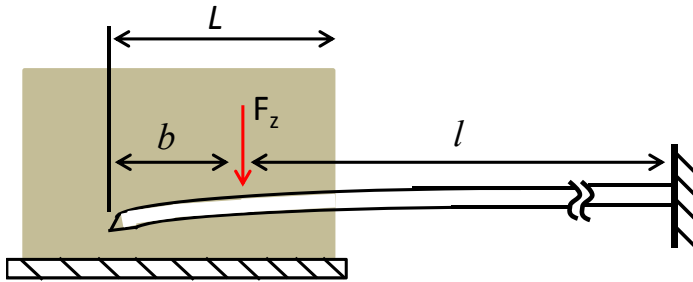
Figure 4.5. Schematic drawing of unknown l and b and how the ratio of b is identified.

The needle length ($b+l$) is a constant (90 mm in this study) and Eq. 4 can be re-arranged to solve the b with given F_z, δ, and L. The F_z is measured by the dynamometer, L can be obtained either by the magnetic tracking sensor or from a constant insertion speed, δ is the deflection measured by the magnetic tracking sensor.

Although it is a single variable problem to solve for b in Eq. 4, the analytical solution is difficult since the highest order of b is three (after replacing l) and the solutions would include both real and imaginary parts. In this study, an optimal searching approach was adopted to find the b which can create the deflection to match with the measured δ at the corresponding insertion depth L.

4.3.4.3 FEA models

The FEA models of the needle and phantom (Fig. 4.2) were created based on the experimental setup and respective dimensions. The needle is made of stainless steel with

the Young's modulus equal to 200 GPa. The fixed-end of needle is applied by the boundary conditions with all six degrees of freedom constrained. The phantom model is a $50\times50\times50$ mm^3 cube with a needle hole at the corresponding insertion position and Young's modulus of 18 kPa. Boundary conditions of the phantom model consisted of: (1) constraining all three translational motions on the phantom bottom, (2) constraining the y-directional motion of the left and right side walls of the phantom, and (3) constraining the x-directional motion on the back wall of the phantom, as illustrated in Fig. 4.6 based on the U-shaped phantom holder support (50 mm in height and 5 mm in width on both sides and 7.5 mm in height in the middle).
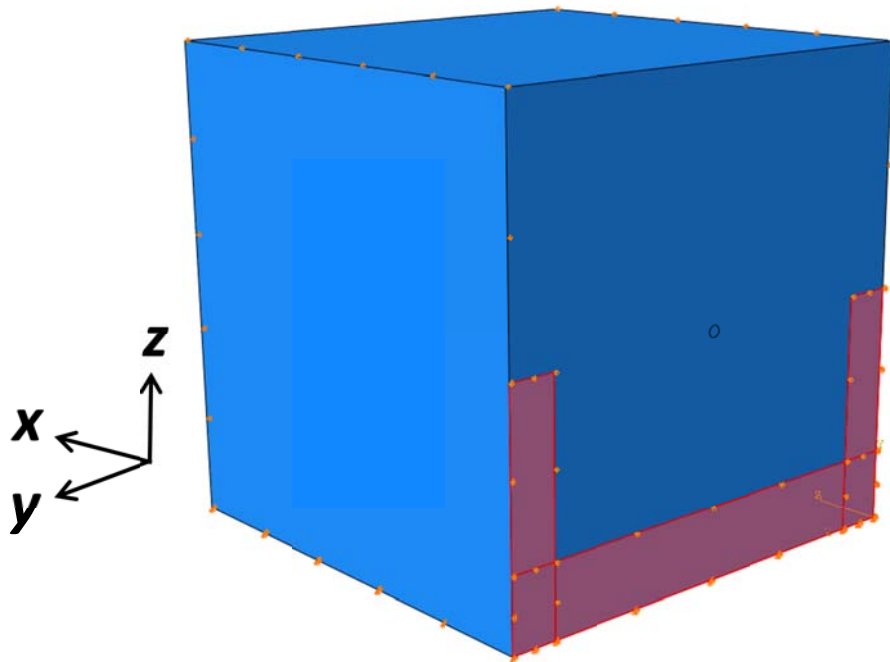
Figure 4.6. The boundary conditions of phantom model with the U-shaped highlighted on the back wall.

4.4 RESULTS AND DISCUSSIONS

This section presents the results of friction and cutting forces, and R (the ratio of b to L) over the 50 mm insertion length. FEA results are shown and validated with experimental measurements.

4.4.1 Friction and cutting forces

Figure 4.7 displays the F_x of two repeated needle insertions into phantom as well as the second subtracted from the first F_x, which is F_f, over the 50 mm insertion distance. As the needle passes through the phantom, the F_f increases gradually like the total axial force. This supports the fact that when the needle length increases within the tissue, the needle-to-phantom contact area and friction force increase. A higher friction force was recorded when the needle length increases during insertion into the phantom. After the needle has travelled 10 mm, the F_c remains relatively constant (from 0.32 to 0.46 N) throughout the needle insertion path. Since most of the cutting of the tissue occurs at the needle tip, the F_c should not increase like the F_f with an increase in the needle-phantom contact.
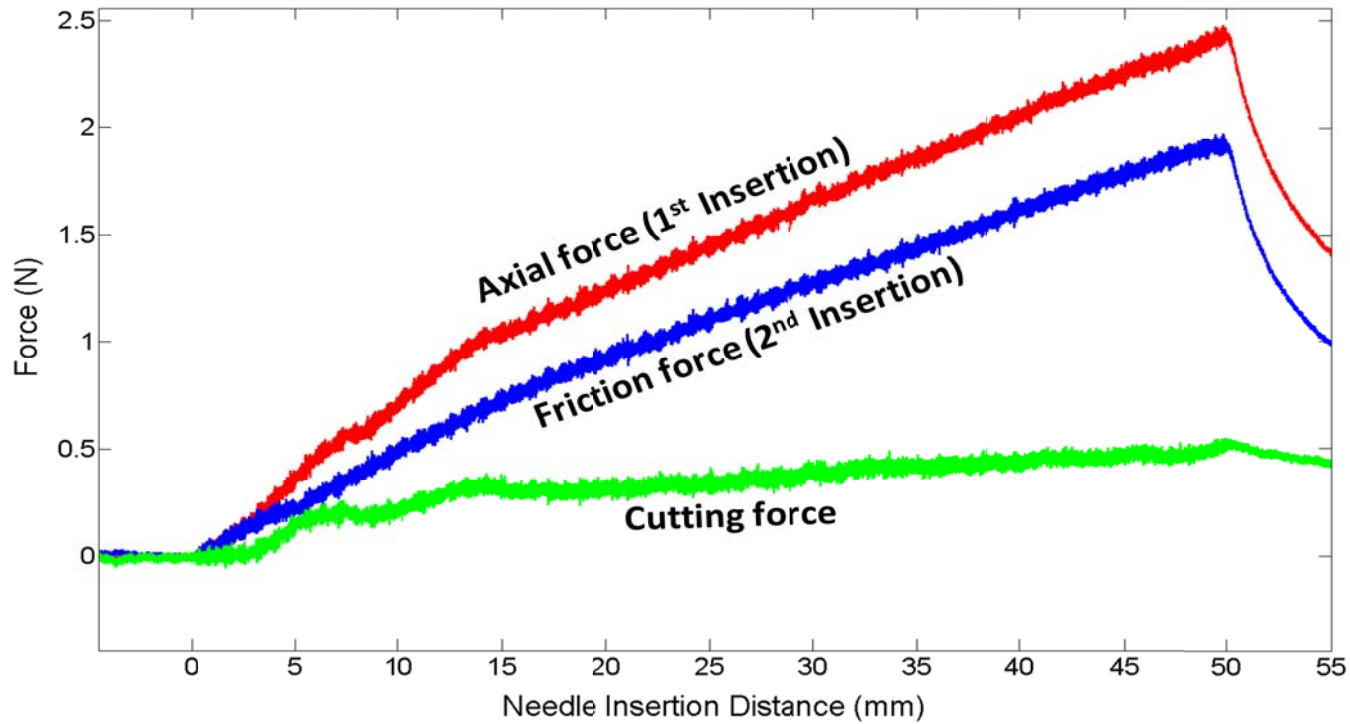
Figure 4.7. Axial force graphs of three data sets - the first needle insertion, the second needle insertion (F_f), and the second subtracted from the first insertion axial force (F_c).

4.4.2 Normal distribution force

Using the method outlined in Section 4.3.4.2, Fig. 4.8 shows the R for two needle-phantom insertion trials. These results were obtained from a separate set of tests (same set-up), compared to the phantom deformation and needle insertion test. The R in the first 32 mm of needle insertion is not stable due to the limited resolution of the magnetic tracking system and its inability to measure needle deflection smaller than 0.5 mm, the rapid increase of force and large initial phantom deformation before the needle penetration also contribute to the inability. After the needle has travelled 32 mm into the phantom, R converges to about 0.6, which is close to the 0.667 and indicates the shape of the force distribution is close to a triangle with peak at the entrance into phantom. For prostate brachytherapy, the first 30 mm after insertion through the skin is not of importance because the prostate is usually located from 60 to 80 mm from the perineum [38]. The ratio of 0.667 was used for the FEA for the placement of F_z to predict the needle deflection.
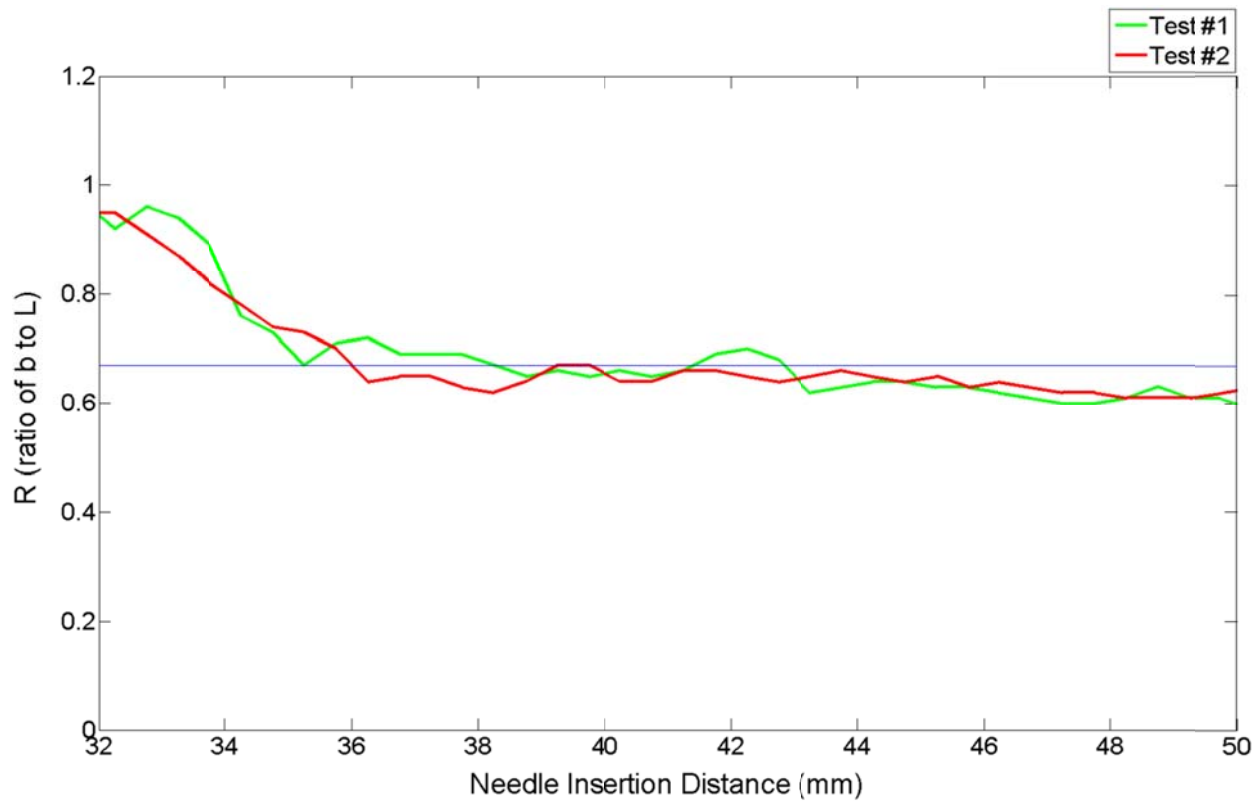
Figure 4.8. Experimental results of R for two tests.

4.4.3 Phantom deformation and needle deflection model

Using the measured F_c, F_f, and F_z as inputs, the phantom deformation and needle deflection can be calculated at each time step during insertion using FEA models proposed in Sections 4.2 and 4.3. Figure 4.9 presents the FEA phantom deformation (with overlaid un-deformed phantom) when the needle is inserted 30 mm into the phantom. The deformation at the top middle surface of the phantom, near the needle insertion face was of interest because it was the location where the miniature sensor was placed within the experimental set-up.

Figure 4.10 shows the FEA results of the deflection of needle, inserted 30 mm into the phantom, along with the overlaid un-deformed needle mesh. The resultant z-directional force (F_z) was placed 20 mm from the needle tip, which 2/3 is the distance from the 30 mm needle insertion length into the phantom. The maximum deflection at the needle tip was of interest to compare to the FEA prediction and experimental measurement using the miniature sensor at the needle tip.
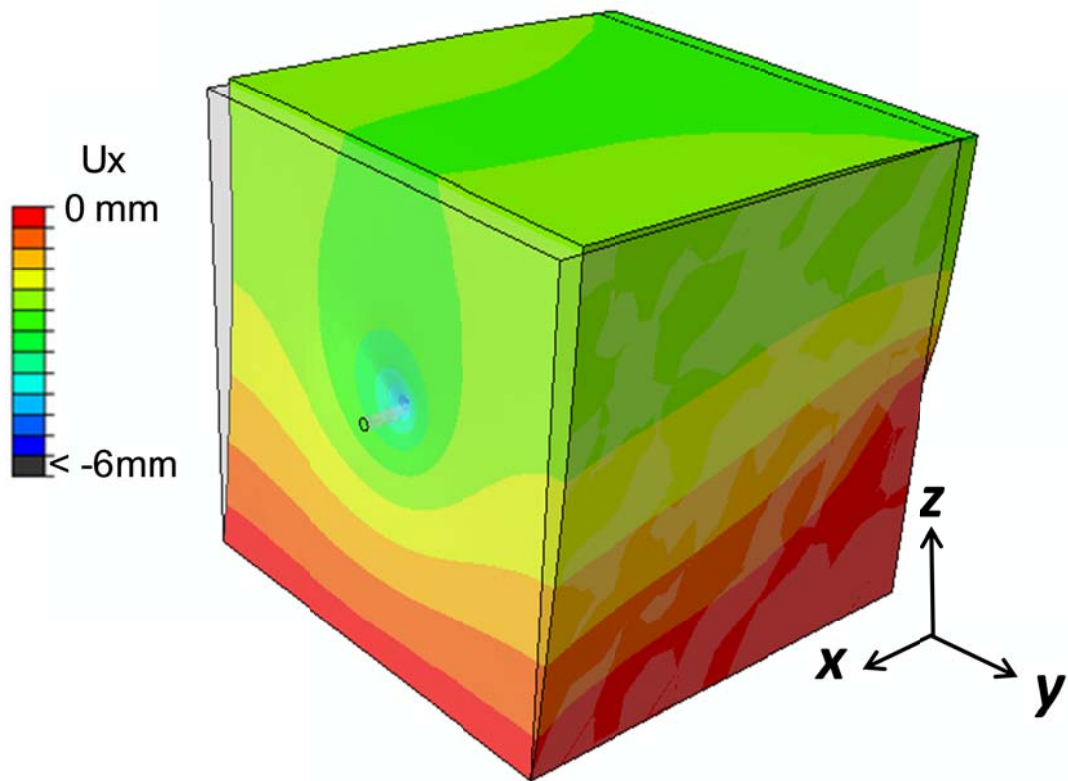
Figure 4.9. FEA model for phantom deformation at 30 mm needle insertion depth, with the overlaid un-deformed phantom. Phantom deformation (in m) occurred in the x-direction.

Figure 4.10. FEA model for needle deflection model at 30 mm needle insertion depth, with the overlaid un-deformed needle. Needle deflection (in m) occurred in the *z*-direction.

Figure 4.11 presents the comparison of sensor measured and FEA predicted needle deflection and phantom deformation results. For needle deflection, results match up well, particularly after the needle has inserted half the total distance of the phantom. For the needle insertion distance smaller than 37 mm, the FEA predicted a slightly higher deflection compared to that of the sensor measurement. This occurs because the actual resultant force at the insertion stage falls at a higher ratio than 0.667 (triangular distribution). As discussed in the Section 4.4.2, one explanation is that before the needle tip penetrates the tissue, a rapid increase in the insertion force occurs at the tip. When the needle enters the phantom, more force is instantaneously exerted on the needle. Thus, a certain amount of insertion distance is needed in order to recover from the initial insertion. During the first 25 mm insertion distance, a higher force is measured by the dynamometer, which does not reflect the actual needle deflection. For the needle insertion distance over 37mm, the FEA prediction is slightly higher. The overall accuracy of the FEA prediction is good and demonstrated the feasibility of the needle deflection FEA model.

For the phantom deformation, the FEA predictions also match well with measurements in the early needle insertion phase (with insertion distance less than 30 mm). The FEA produced a higher phantom deformation than the phantom sensor measurements. One justification for this difference could be the FEA boundary conditions. The entire bottom of the phantom was stationary (fixed). However, during the experiment, it is possible that the phantom can slide a small distance in the needle insertion direction and would result in a smaller overall phantom deformation for the phantom sensor. Another possibility for the discrepancy is the nonlinear Young Modulus of the soft PVC under large strain. We used the value of 18 kPa, measured using indentation test, thus it may not be an accurate measurement.
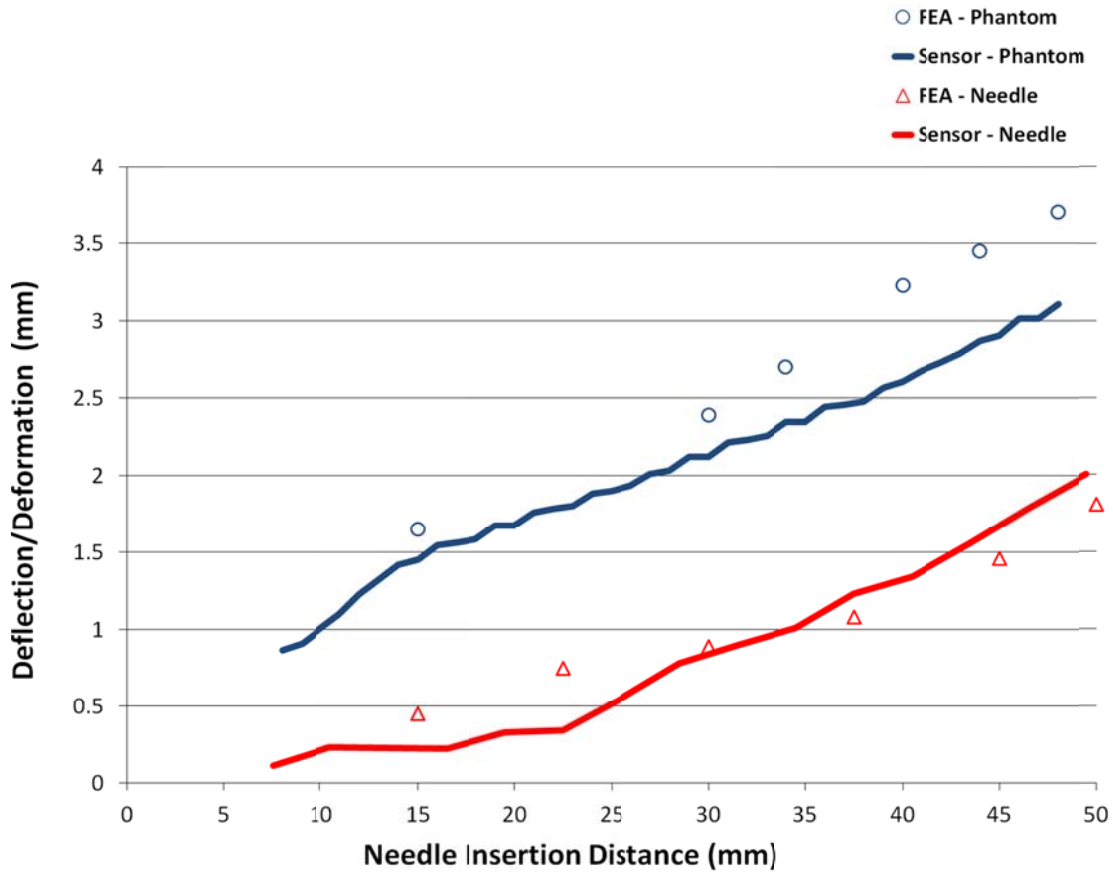
Figure 4.11. Comparison of the FEA and measurements of the phantom deformation and needle deflection.

To study the effect of F_x on needle deflection, a comparison test was performed to see how much of an effect F_x contributes to needle deflection. The needle FEA [Fig. 4.2(a)] with two conditions were generated – one with both F_x and F_z and the other with F_z only. The analysis results of L at 30 mm and 50 mm both showed that the needle deflection difference between the two conditions was less than 5%.

4.5 CONCLUSIONS

This research presented a concept of using forces measured during needle insertion into tissue as inputs for FEA to predict the needle deflection and phantom deformation. This approach was validated via comparison with non-contact magnetic

tracking sensors embedded in the needle and phantom for experimental measurements. The normal force distribution was studied experimentally and demonstrated to be triangular in shape with the peak at the entrance into phantom. This assumption had been proposed previously in the literature [19-21] and was validated in this study.

Results and approach presented in this study can be translated to the robotic needle insertion for brachytherapy procedures. If the target location and tissue properties are known, a robotic device can be program to apply the required force needed to follow a certain path and place the needle tip at the target location. A major limitation of this study is the use of a homogenous phantom instead of a heterogeneous tissue for experiments. However, understanding the needle-tissue interaction, such as the triangular normal force distribution, was of importance. Future work includes using the animal model to study the needle deflection and phantom deformation over an insertion distance and comparing to the experimental measurements and homogenous phantom insertion results. Additionally, investigation could be conducted to study the needle insertion speed effects on needle and phantom movement to find the optimal needle insertion speed to minimize needle deflection and phantom deformation.

REFERENCES

1. J. Moore, C. Clarke, D. Bainbridge, C. Wedlake, A. Wiles, D. Pace, and T. Peters, "Image Guidance for Spinal Facet Injections Using Tracked Ultrasound," *Proceedings of the 12th International Conference on Medical Image Computing and Computer-Assisted Intervention* – MICCAI (London, England, 2009), pp. 516-223.

2. H. Xu, A. Lasso, S. Vikal, P. Guion, A. Krieger, A. Kaushal, L. L. Whitcomb, and G. Fichtinger, "MRI-Guided Robotic Prostate Biopsy: A Clinical Accuracy Validation," *Proceedings of the 13th International Conference on Medical Image Computing and Computer-Assisted Intervention* – MICCAI (Beijing, China, 2010), pp. 383-391.

3. S. Song, N. B. Cho, G. Fischer, N. Hata, C. Tempany, G. Fichtinger, and I. Iordachita, "Development of a Pneumatic Robot for MRI-guided Transperineal Prostate Biopsy and Brachytherapy: New Approaches," *IEEE International Conference on Robotics and Automation*, (Anchorage, Alaska, 2010), pp. 2580-2585.

4. A. T. Porter, J. C. Blasko, P. D. Grimm, S. M. Reddy, and H. Ragde, "Brachytherapy for Prostate Cancer," CA: A Cancer Journal for Clinicians **45**, 165-178 (1995).

5. J. C. Blasko, "Brachytherapy," Urology **55**, 306-308 (2000).

6. S. Nath, Z. Chen, N. Yue, S. Trumpore, and R. Peshcel, "Dosimetric effects of needle divergence in prostate seed implant using ^{125}I and ^{103}Pd radioactive seeds," Medical Physics **27**, 1058-1066 (2000).

7. N. N. Stone and R. G. Stock, "Complications Following Permanent Prostate Brachytherapy," European Urology **41**, 427-433 (2002).

8. J. C. Blasko, T. Mate, J. E. Sylvester, P. D. Grimm, and W. Cavangah, "Brachytherapy for Carcinoma of the Prostate: Techniques, Patient Selection, and Clinical Outcomes," Seminars in Radiation Oncology **12,** 81-94 (2002).

9. T. Azar and V. Hayward, "Estimation of the Fracture Toughness of Soft Tissue from Needle Insertion," Biomedical Simulation **5104,** 166-175 (2008).

10. M. Mahvash and P. E. Dupont, "Mechanics of Dynamic Needle Insertion into a Biological Material," IEEE Transactions on Biomedical Engineering **57**, 934-943 (2010).

11. O. A. Shergold and N. A. Fleck, "Experimental Investigation Into the Deep Penetration of Soft Solids by Sharp and Blunt Punches, With Application to the Piercing of Skin," Journal of Biomechanical Engineering **127**, 838-848 (2005).

12. O. A. Shergold and Norman A. Fleck, "Mechanisms of deep penetration of soft solids, with application to the injection and wounding of skin," Proceedings of the royal society A **460,** 3037-3058 (2004).

13. M. Mahvash and V. Hayward "Haptic Rendering of Cutting: A Fracture Mechanics Approach," Haptics-e **2**, 1-12 (2001).

14. M. Okamura, C. Simone, and M. D. O'Leary, "Force modeling for needle insertion into soft tissue," IEEE Transactions on Biomedical Engineering **51,** 1707-1716 (2004).

15. Y. Kobayashi, T. Sato, and M. G. Fujie, "Modeling of friction force based on relative velocity between liver tissue and needle for needle insertion simulation," *31st Annual International Conference of the IEEE Engineering in Medicine and Biology Society*, (Minneapolis, MN, 2009), pp. 5274-5278.

16. H. Kataoka, T. Washio, K. Chinzei, K. Mizuhara, C. Simone, and A. M. Okamura, "Measurement of the tip and friction force acting on a needle during penetration," *Proceedings of the 5th International Conference on Medical Image Computing and Computer-Assisted Intervention* — MICCAI (Tokyo, Japan, 2002), pp. 216-223.

17. N. Abolhassani, R. Patel, and M. Moallem "Experimental study of robotic needle insertion in soft tissue." International Congress Series **1268**, 797-802 (2004).

18. S. P. DiMaio and S. E. Salcudean "Needle insertion modeling and simulation," IEEE Transactions on Robotics and Automation **19**, 864–875 (2003).

19. N. Abolhassani and R. V. Patel, "Deflection of a Flexible Needle during Insertion into Soft Tissue," 28th *Annual International Conference of the IEEE Engineering in Medicine and Biology Society*, (New York City, USA, 2006), pp. 3858 -3861.

20. N. Abolhassani, R. V. Patel, and F. Farzam, "Minimization of needle deflection in robot-assisted percutaneous therapy," The International Journal of Medical Robotics and Computer Assisted Surgery **3**, 140-148 (2007).

21. N. Abolhassani, R. V. Patel, and F. Ayazi, "Needle control along desired tracks in robotic prostate brachytherapy," IEEE International Conference on Systems, Man and Cybernetics, (Montreal, Canada, 2007), pp. 3361-3366.

22. S. Misra, K. B. Reed, B. W. Schafer, K. T. Ramesh, and A. M. Okamura, "Observations and models for needle-tissue interactions," *IEEE International Conference on Robotics and Automation*, (Kobe, Japan, 2009), pp. 2687-2692.

23. S. Misra, K. B. Reed, B. W. Schafer, K. T. Ramesh, and A. M. Okamura, "Mechanics of flexible needles robotically steered through soft tissue." The International Journal of Robotics Research **29,** 1640-1660 (2010).

24. A. Asadian, M. R. Kermani, and R. V. Patel, "An analytical model for deflection of flexible needles during needle insertion," IEEE/RSJ International Conference on Intelligent Robots and Systems, (San Francisco, USA, 2011), pp. 2551-2556.

25. D. Glozman and M. Shoham, "Flexible needle steering and optimal trajectory planning for percutaneous therapies," *Proceedings of the 7th International Conference on Medical Image Computing and Computer-Assisted Intervention –* MICCAI (Saint-Malo, France, 2004), pp. 137-144.

26. D. Glozman and M. Shoham, "Flexible needle steering for percutaneous therapies." Computer Aided Surgery **11**, 194 – 201 (2006).

27. R. J. Roesthuis, Y. R. J. van Veen, A. Jahya, and S. Misra, "Mechanics of needle-tissue interaction," IEEE/RSJ International Conference on Intelligent Robots and Systems (IROS), (San Francisco, USA, 2011), pp. 2557-2563.

28. S. Misra, K. T. Ramesh and A. M. Okamura, "Modeling of tool-tissue interactions for computer-based surgical simulation: A literature review," Presence: Teleoperators and Virtual Environments **17**, 463-491 (2008).

29. N. Abolhassani, R. Patel, and M. Moallem, "Needle insertion into soft tissue: A survey." Medical Engineering & Physics **29**, 413-431 (2007).

30. E. Dehghan and S. E. Salcudean, "Needle Insertion Study Using Ultrasound-Based 2D Motion Tracking,*" Proceedings of the 11th International Conference on Medical Image Computing and Computer-Assisted Intervention –* MICCAI (New York City, USA, 2008), pp. 660-667.

31. J. R. Crouch, C. M. Schneider, J. Wainer, and A M. Okamura, "A Velocity-Dependent Model for Needle Insertion in Soft Tissue," *Proceedings of the 8th International Conference on Medical Image Computing and Computer-Assisted Intervention – MICCAI* (Palm Springs, USA, 2005), pp. 624-632.

32. A. Haddadi and K. Hashtrudi-Zaad, "Development of a dynamic model for bevel-tip flexible needle insertion into soft tissues," *3rrd Annual International Conference of the IEEE Engineering in Medicine and Biology Society*, (Boston, USA, 2011), pp. 7478 -7482.

33. H. Kataoka, T.Washio, M. Audette, and K. Mizuhara, "A Model for relations between needle deflection, force, and thickness on needle penetration," *Proceedings of the 4th International Conference on Medical Image Computing and Computer-Assisted Intervention*, (Utrecht, The Netherlands, 2001), pp. 966–974.

34. T. K. Podder, D. P. Clark, J. Sherman, D. Fuller, E. Messing, D. J. Rubens, J. G. Strang, Y. D. Zhang, W. O'Dell, W. S. Ng, and Y. Yu, "Effects of tip geometry of surgical needles: an assessment of force and deflection," *Third European Medical and Biological Engineering Conference* (Prague, Czech Republic, 2005), pp. 1641-1644.

35. Y. Yu, T. K. Podder, Y. Zhang, W. S. Ng, V. Misic, J. Sherman, L Fu, D. Fuller, E. Messing, D. Rubens, J. Strang, and R. Brasacchio, "Robot-Assisted Prostate Brachytherapy" *Proceedings of the 9th International Conference on Medical Image Computing and Computer-Assisted Intervention – MICCAI* (Copenhagen, Denmark, 2006), pp. 41-49.

36. C. S. McGill, J. A. Schwartz, J. Z. Moore, P. W. McLaughlin, and A. J. Shih, "Precision grid and hang motion for accurate needle insertion in brachytherapy," Medical Physics **38**, 4749-4759 (2011).

37. C. S. McGill, J. A. Schwartz, J. Z. Moore, P. W. McLaughlin, and A. J. Shih, "Effects of insertion speed and trocar stiffness on the accuracy of needle position for brachytherapy," Medical Physics **39**, 1811-1817 (2012).

38. L. Fu, W. S. Ng, H. Liu, W. O'Dell, D. Rubens, J. Strang, M. C. Schell, R. Brasacchio, L. Liao, E. Messing, and Y.Yu, "Bouquet brachytherapy: feasibility and optimization of conically spaced implants," Brachytherapy **4,** 59-63 (2005).

CHAPTER 5

CONCLUSIONS AND FUTURE WORK

5.1 CONCLUSIONS

Decreasing needle deflection is essential for the needle tip to accurately place radioactive seeds into the cancerous cells target location for optimal dosage. While much work has been achieved on slow needle insertion speed and axial - needle insertion direction - force distribution, little work has been performed on stiffer needle material properties, tissue deformation with needle deflection, and normal - perpendicular to needle insertion direction - force distribution. This lack of knowledge have led to tissue deformation, needle deflection, and misplaced target when performing needle insertion procedures. This dissertation aims to fulfill some of the gap of needle stiffness properties, optimizing equipment, needle normal (perpendicular to insertion direction) force distribution, and simultaneously studying needle deflection and phantom deformation during insertion. The results from this dissertation enhance the understanding of the effect each parameters and insertion techniques have on needle deflection. The results from this dissertation can be used to understand the needle insertion techniques and force distribution effect on needle bending, and compensate during the insertion path.

The major achievements of this dissertation are:

- *Effect of improved needle grid and datum stand measurement system:* A 18-gauge needle grid was constructed to decrease the diametral clearance

between the inside hole and outside diameter of the (18-gauge) needle from 76 μm to 33 μm, in addition to increasing the travel length of the grid by 30 mm. Additionally, a measurement apparatus (datum stand and digital depth gauge) was developed to measure the final vertical and horizontal needle deflection. This measurement apparatus has acceptable gauge repeatability and reproducibility (GR&R) measurement and documented accuracy on needle deflection measurements. Results showed that the grid with tight clearance holes decreased average needle deflection for slow speed insertion by 30% and decreased average needle deflection for fast (quick flick of the wrist) insertion speeds by 40%. However, increased grid length was not as significant to needle deflection. This tight clearance grid provided a more accurate needle placement before needle tip penetration into the phantom.

- *Pneumatic insertion speed and stiffer needle:* A pneumatic insertion device was developed to produce speeds over 2500 mm/s, over a 150 mm insertion distance. Additionally, a stiffer needle was constructed by replacing the inner stainless steel (SS) portion of the needle (trocar) with a tungsten carbide with 6% cobalt material. With a Young's modulus over three times SS, the trocar was inserted into the cannula, before insertion with the pneumatic device. Results showed that the average needle deflection decreased by 60% when the stiffer needle was inserted at the higher speed, compared to the SS needle inserted at the slower speed. This device enabled accurate needle insertion at speeds much faster than hand insertion or current robotic devices in the literature.

- *Needle and phantom force models, and normal force distribution:* Needle deflection and phantom deformation finite element analysis (FEA) force models were developed to predict relative motion during the entire needle path. Using experimental input force data, needle and phantom FEA models are reasonably accurate to experimental data, 7% and 18%, respectively at the worst data point, after validation with measured needle deflection and phantom deformation data. Additionally, the normal force distribution of triangle with the peak portion near the needle entrance side was validated

with an additional set of measured experimental needle-phantom results. The knowledge gained can be implemented on robotic needle device in which forces during needle insertion are measured for compensation in order to achieve the desired target.

The original contributions of this research are as follows:

1. Develop a needle grid with tight clearance holes used to guide the needle before penetration into the phantom. This grid has great potential for implantation into the operating room to use during actually prostate brachytherapy procedures. A 40% decrease in average needle deflection occurred with the tight clearance hole grid and the same fast hand insertion technique.

2. Implement a measurement apparatus with acceptable gauge repeatability and reproducibility (GR&R) measurement and documented accuracy on needle deflection measurements. This measurement apparatus can measure final needle deflection without using an imaging device.

3. Introduce pneumatic needle insertion as a method to produce much faster insertion speed than hand insertion or current robotic devices in the literature.

4. Incorporated a higher Young's modulus material (tungsten carbide with 6% cobalt) for the trocar in other to make the needle stiffer. A 60% decrease in average needle deflection occurred when the stiffer needle was inserted at the higher pneumatic speed.

5. Develop a FEA model which incorporates force inputs from the study while simultaneously obtaining tissue-phantom interaction forces, needle deflection, and phantom deformation for the entire needle insertion path. The FEA model was validated from the measured needle deflection and phantom deformation data. The needle and phantom FEA models are reasonably accurate to the experimental data, having a difference of 7% and 18%, respectively.

6. Validate the normal force distribution of triangle with the peak portion near the needle entrance side.

5.2 FUTURE WORK

The methodologies, equipment, and models introduced in this dissertation could be expanded through the following research:

1. Develop a model which will correlate the high needle insertion speed, via the pneumatic device, to a trajectory when a specified needle material, insertion distance, and tissue property is known. Additionally, an optimal needle insertion speed can be achieved to produce the smallest needle deflection.
2. Explore other needle properties, such as the cannula material and wall thickness, to optimize the needle and produce accurate insertion.
3. Incorporate fiducial markers into tissue phantom and study the effect needle insertion into different areas (in relation to boundary conditions) have on marker and target displacement and
4. Investigate the effect of normal and axial forces on needle deflection and phantom deformation when the needle bevel angle is varied.
5. Compare the needle-phantom (homogeneous) finite element model to needle-tissue (heterogeneous) force model.
6. Use miniature sensors to continue investigating tight clearance hole grid, needle properties, and high-speed needle insertion technique in order to study the needle path during insertion.

APPENDICES

APPENDIX A

SAMEPLE SIZE AND OUTLIERS

A.1 Sample size

In order to calculate the sample size [1], equation (A.1) for a fixed effects experiment was used. Equation (A.1) uses Φ and the operating characteristic curve (α = 0.05) to find the number of replicates to use in the experiment that will be sensitive to the important differences in the conditions. Using a power (probability of rejecting the null hypothesis, with the null hypothesis being the difference between any two conditions mean is 1 mm, when the null is false) of at least 0.85 was used to find the sample size of n = 10 replicates for this experiment.

$$\Phi^2 = \frac{nD^2}{2a\sigma^2} \tag{A.1}$$

where Φ^2 is a parameter that related to the non-centrality parameter, n is the number of replicates, D is the difference between any two conditions means, a is the number of levels for the factors, and σ^2 is the variance. A difference between conditions of D = 1 mm, a = 2 levels, and a variance σ^2 = 0.49 mm^2 were used in equation (A.1). The variance was obtained from a previous experiment when two operators and 3 measurement trials were used to obtain the value.

A.2 Outliers

Outliers within each condition combinations were detected using Grubbs' test [2,3]. Grubbs' test uses the extreme studentized deviate (ESD) method to quantify how far outliers are from the other data points by using the following equation

$$Z = \frac{|\mu - v|}{\sigma} \tag{A.2}$$

where Z is the ratio used to compare to the critical value, μ is the mean of the data points within a condition combination, v is the replicate of interest within the condition, and σ is the standard deviation of the data points within a condition combination. If Z is bigger than 2.29 (the critical value when the sample size is 10) [2,3], the value used to calculate Z is an outlier (p-value < 0.05). This method, which uses a two-sided t-test, states that the chances are less than 5% that you encountered an outlier by chance alone, if data were sampled from a Gaussian distribution.

REFERENCES

1. D. C. Montgomery, *Design and Analysis of Experiments* (Wiley, New York, 2005).

2. V. Barnett and T. Lewis, *Outliers in Statistical Data* (John Wiley & Sons, New York, 1994).

3. B. Iglewicz and D. C. Hoaglin, *How to Detect and Handle Outliers* (American Society for Quality Control, Wisconsin, 1993).

APPENDIX B

MAGNETIC POSITION TRACKING SYSTEM: SENSOR DYNAMIC ACCURACY AND FERROUS MATERIAL INTERFERENCE TEST

B.1 MATERIALS AND METHOD

B.1.1 Sensor dynamic accuracy test

For the first part of the sensor dynamic accuracy experiment test, one sensor was placed inside the tip of a hollow 18-gague stainless steel cannula. The cable which connects the sensor to the TrackSTAR electronic unit was taped at the distal end of the needle to minimized sensor movement within the cannula. The transmitter, with side 1 facing the needle in the x-direction (Fig. B.1), was placed approximately 20 cm away from the sensor. No phantom was present during this test. The linear stages were used to create individual horizontal (x-direction), vertical (z-direction), and lateral (y-direction) stepping motion at a speed of 1.5 mm/s, in increments of 1 mm and 0.5 mm stepping motion. These small increments were chosen because Ascension's published accuracy for the system is 0.5 mm. The stepping motion consisted of 10 steps in the positive coordinate direction and then 10 steps in the negative coordinate direction, with each step remaining in that position for 2 seconds. This procedure was repeated three times for a total of 60 steps per trial. The Ascension's proprietary Cubes program was used to record the position data while MATLAB software (Natick, MA) and Microsoft Excel software (Redmond, WA) were used for analysis purposes.

The second part of the sensor dynamic accuracy experiment test consisted of testing the accuracy effect of having the needle/sensor tip pointed and parallel to sides 1–

4 of the transmitter (Fig. B.1). The transmitter was rotated in order to have each side (1–4) of the transmitter face (or parallel to) the needle/sensor tip while having the vertical (z-direction) linear stage perform stepping motions in increments of 1 mm and 0.5 mm. Four sets of data were recorded for each face, two z-directional linear stage stepping motion at a speed of 1.5 mm/s with the sensor pointed directly at the transmitter cube (1 mm and 0.5 mm steps) and two z-directional linear stage stepping motion at a speed of 1.5 mm/s with the sensor parallel to the transmitter face (1 mm and 0.5 mm steps). For each trial, the stepping motion consisted of 10 steps in the positive coordinate direction and then 10 steps in the negative coordinate direction, with each step remaining in that position for 2 seconds. This procedure was also repeated three times for a total of 60 steps per trial.

Analysis for both parts of the experiment for the sensor dynamic accuracy consisted of taking the averages of all the data within the 2 second time period when the linear stage was stationary per stepping motion. Next, the previous step average was subtract from the current step average (i.e.: the average of 1.5 mm step was subtracted from the current 2.0 mm step when preforming the 0.5 mm incremental stepping motion), in order to obtain the actual distance the sensor travelled per stepping motion. The total averages of each average stepping motion and the standard deviation of the averages were obtained for each part of the sensor dynamic accuracy test.

B.1.2 Sensor ferrous material interference test

The second experiment is to test the interference effect of ferrous material on the magnetic field via a stationary sensor test. This set-up consisted of one sensor taped to the wooden table, and placed 20 cm away from the transmitter. After recording the position data of the stationary sensor for 10 seconds via the Ascension's Cubes program, a permanent magnet was brought into the magnetic field to change the quality reading in the Cubes program. The quality reading is a discrete value calculated by the Ascension's Cubes program, which determines the level of interferences in the magnetic field. The magnet was moved towards the sensor until the desired quality measurement was

reached, followed by recording ten seconds of data without moving the sensor, transmitter, or permanent magnet. Data was recorded for quality values from 0 to 5, with the best quality value having a value of 0. Sides 1-4 (Fig. B.1) of the transmitter were used within this experiment.

Analysis for this experiment consisted of taking the *z*-position data averages and standard deviation of all the data within the 10 second time period, per quality value and transmitter side. Next, for each quality discrete value, the 0 quality average value was subtracted from the other quality values (1-5) average *z*-position data, for the respective transmitter side. This test compares how the average *z*-position data per quality value differ from the idea quality value (value of 0) per transmitter side.
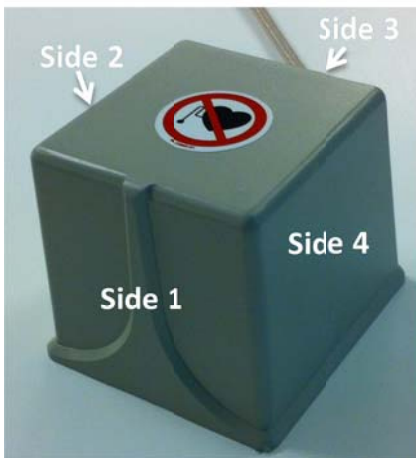

Figure B.1. Numbering convention for each side of the transmitter used for the sensor's dynamics accuracy test and the ferrous material interference test.

## B.2 RESULTS AND DISCUSSIONS

The 3D Guidance TrackSTAR's sensor dynamic accuracy and the ferrous material interference effect on the magnetic field results are shown and discussed below.

B.2.1 Sensor dynamic accuracy test

Results for the first part of the sensor dynamic accuracy test, where the needle/sensor tip faces side 1 of the transmitter and the three linear stages were individually moved in 1 mm and 0.5 mm stepping motions, are shown in Table B.1. The average shows how accurate the system measured the movement and the standard deviation shows the precision of repeated measurements. Accurate measurements are values closer to the actual step size of the linear stages, either 1 mm or 0.5 mm depending on the input stepping motion. Precise measurement has the smallest values for the standard deviation. As presented in Table B.1, the x-directional and the z-directional 1 mm stepping motion both have a 0.009 mm difference from the target 1 mm. However, the x-directional motion has the smallest standard deviation for the 1 mm and 0.5 mm stepping motion and the smallest average step size difference from the 0.5 mm input stepping motion. The y-directional 0.5 mm stepping motion did not produce discrete stepping data in order to distinguish and compare values between each step. Thus, the y-directional 0.5 mm stepping data is not presented. Overall, the x-directional stepping motion produced the best results for average step size and standard deviation values for both the 1 mm and 0.5 mm stepping motion test. One explanation is that the x-directional tests always points at the front cube face, while the y-directional and z- directional step tests were always parallel to the cube face. Thus, when the stepping motion was applied to each directional linear stages, the x-directional motion would move closer and then back from the transmitter, while both the y-directional and z- directional stepping motion does not move as close to the transmitter, when compared to the x-directional motion. Thus, the second set of sensor dynamic accuracy test was performed in order to test the effect of the sensor orientation (parallel and facing each transmitter side) has on the accuracy and standard deviation values.

Table B.1. Results of the three linear stages stepping motion facing transmitter side 1

Linear stage motion	1 mm		0.5 mm	
	Avg. step size (mm)	Standard deviation (mm)	Avg. step size (mm)	Standard deviation (mm)
x-direction	1.009	0.028	0.503	0.038
y-direction	0.908	0.070	N/A	N/A
z- direction	0.991	0.061	0.496	0.063
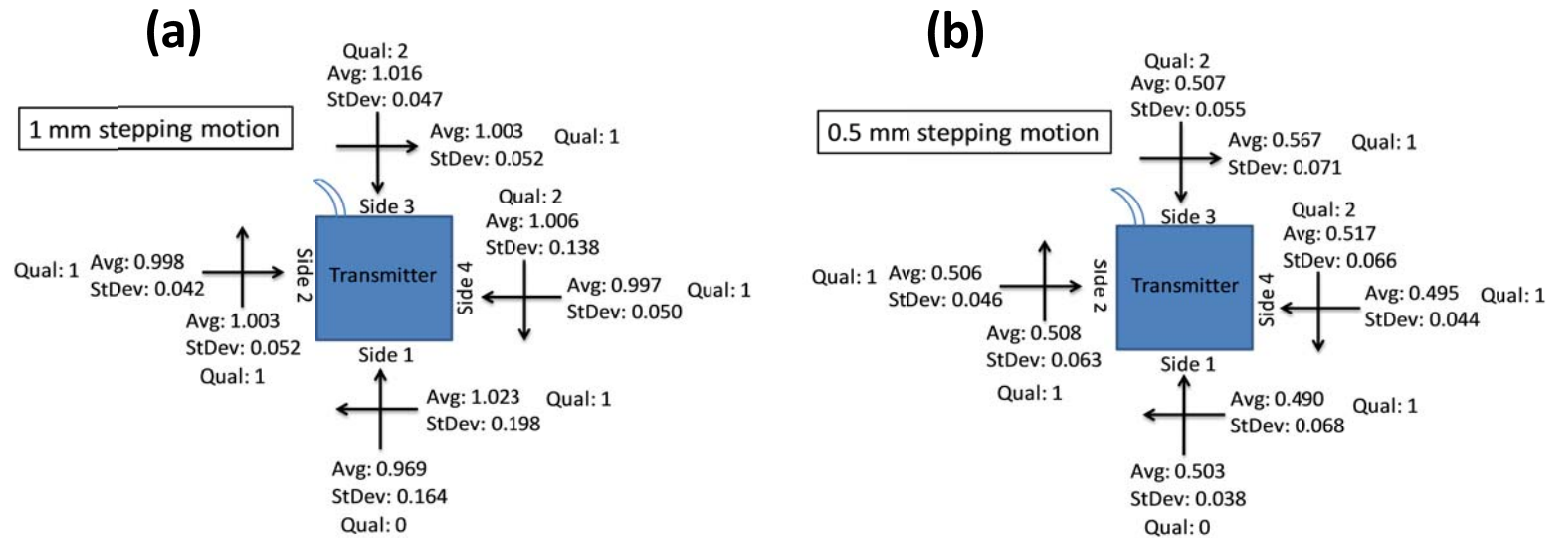
Figure B.2. Results of z-directional linear stage, sensor dynamic accuracy per transmitter side with (a) 1 mm stepping motion and (b) 0.5 mm stepping motion.

The second part of the sensor dynamic accuracy test results, where the z-directional linear stage stepping motion with the needle/sensor tip pointed to and parallel to sides $1 - 4$ of the transmitter, are presented in Fig. B.1. For the 1 mm stepping motion test [Fig. B.2(a)], the standard deviation values were smaller when the sensor was pointed at the transmitter. Thus, measurements collected while the sensor was pointed at the transmitter are more precise than when the sensor was parallel to the transmitter face. On the contrary, the calculated averages did not provide unanimous information in order to make a definitive conclusion about one orientation having better results than the other. For the 0.5 mm stepping motion test [Fig. B.2(b)], the standard deviation and averages values when the sensor was orientated towards the transmitter were better compared to when the sensor was in parallel. The difference between the average and the input 0.5 mm stepping motion were smaller when the sensor was pointed towards the transmitter. Additionally, side 1 produced the smallest standard deviation value and smallest average difference compared to the other three sides, when the sensor is pointed to that side.

B.2.2 Sensor ferrous material interference test

Results for the ferrous material interference test, where the sensor was taped to the wooden table and a permanent magnet was brought into the magnetic field, are shown in Table B.2. As shown in Table B.2, the standard deviations of the data between the three transmitter sides within each quality value were similar. There was not a huge numerical difference between the lowest and highest transmitter side's standard deviation value for a respective quality value. However, there was a difference in average z-position values between the three transmitter sides when the quality level increases (decreasing the quality). As the quality value increases, from the ideal 0 value, an offset error was added to the data. Also, transmitter side 2 tends to have the highest offset from quality 0 for all test performed at qualities 1–5, within Table B.2. Transmitter side 3 (the back of the cube) was not included in the results because the numbers were not close to the other three transmitter sides for a respective quality value.

106

Table B.2. Ferrous material stationary position test comparing different sides of the transmitter

Quality	Transmitter side	Average z-position (mm)	Offset from 0 quality (mm)	Standard deviation (mm)
0	1	41.277	-	0.055
	2	41.122	-	0.075
	4	42.478	-	0.060
1	1	41.895	0.618	0.060
	2	42.192	1.070	0.064
	4	43.108	0.630	0.064
2	1	42.476	1.199	0.060
	2	42.988	1.866	0.065
	4	43.665	1.187	0.065
3	1	43.749	2.472	0.054
	2	44.601	3.479	0.061
	4	44.732	2.254	0.059
4	1	45.144	3.867	0.063
	2	46.019	4.897	0.064
	4	46.002	3.524	0.061
5	1	46.093	4.816	0.058
	2	46.923	5.801	0.063
	4	46.985	4.507	0.054